Earth Syst. Dynam., 4, 267–286, 2013
www.earth-syst-dynam.net/4/267/2013/
doi:10.5194/esd-4-267-2013

Earth System Dynamics
Open Access

Variation in emission metrics due to variation in CO_2 and temperature impulse response functions

D. J. L. Olivié[1,2] **and G. P. Peters**[1]

[1]Center for International and Environmental Climate Research – Oslo (CICERO), Oslo, Norway
[2]Department of Geosciences, University of Oslo, Oslo, Norway

Correspondence to: D. J. L. Olivié (dirk.olivie@geo.uio.no)

Received: 30 July 2012 – Published in Earth Syst. Dynam. Discuss.: 3 September 2012
Revised: 8 May 2013 – Accepted: 30 June 2013 – Published: 8 August 2013

Abstract. Emission metrics are used to compare the climate effect of the emission of different species, such as carbon dioxide (CO_2) and methane (CH_4). The most common metrics use linear impulse response functions (IRFs) derived from a single more complex model. There is currently little understanding on how IRFs vary across models, and how the model variation propagates into the metric values.

In this study, we first derive CO_2 and temperature IRFs for a large number of complex models participating in different intercomparison exercises, synthesizing the results in distributions representing the variety in behaviour. The derived IRF distributions differ considerably, which is partially related to differences among the underlying models, and partially to the specificity of the scenarios used (experimental setup).

In a second part of the study, we investigate how differences among the IRFs impact the estimates of global warming potential (GWP), global temperature change potential (GTP) and integrated global temperature change potential (iGTP) for time horizons between 20 and 500 yr.

Within each derived CO_2 IRF distribution, underlying model differences give similar spreads on the metrics in the range of −20 to +40 % (5–95 % spread), and these spreads are similar among the three metrics.

GTP and iGTP metrics are also impacted by variation in the temperature IRF. For GTP, this impact depends strongly on the lifetime of the species and the time horizon. The GTP of black carbon shows spreads of up to −60 to +80 % for time horizons to 100 yr, and even larger spreads for longer time horizons. For CH_4 the impact from variation in the temperature IRF is still large, but it becomes smaller for longer-lived species. The impact from variation in the temperature IRF on iGTP is small and falls within a range of ±10 % for all species and time horizons considered here.

We have used the available data to estimate the IRFs, but we suggest the use of tailored intercomparison projects specific for IRFs in emission metrics. Intercomparison projects are an effective means to derive an IRF and its model spread for use in metrics, but more detailed analysis is required to explore a wider range of uncertainties. Further work can reveal which parameters in each IRF lead to the largest uncertainties, and this information may be used to reduce the uncertainty in metric values.

1 Introduction

Emission metrics are routinely used as a simple means of comparing the climate impact of the emission of various species. The most common emission metric is the global warming potential (GWP), but the global temperature change potential (GTP) has received considerable attention more recently (Fuglestvedt et al., 2003; Aamaas et al., 2013). Both these metrics compare the climate impact of the pulse emission of a certain species with the impact of the pulse emission of the same amount of carbon dioxide (CO_2). The GWP compares the radiative forcing (RF) integrated from the time of emission until a specified time, the so-called time horizon (Shine et al., 1990), while the GTP compares the global-mean temperature change at a certain time after the emission (Shine et al., 2005). More recently, an integrated version of GTP was presented (iGTP), and this compares the temperature change integrated from the time of emission until a time horizon (Gillett and Matthews, 2010; Peters et al., 2011; Azar and Johansson, 2012). It is found that iGTP and GWP are

similar, with one quantifying the energy added to the system (GWP), and the other quantifying the energy lost (iGTP) (Peters et al., 2011; Azar and Johansson, 2012).

Together with the climate impact to be evaluated, the time horizon is an important quantity affecting the metric values (Fuglestvedt et al., 2003; Aamaas et al., 2013). Frequently used time horizons are 20, 100, and 500 yr for GWP, and 20, 50, and 100 yr for GTP (Fuglestvedt et al., 2003, 2010; Shine et al., 2005, 2007). A GWP with a 100 yr time horizon is by far the most common emission metric due to its application in climate policies such as the Kyoto Protocol.

Emission metrics generally condense the complex behaviour of the climate response into a simple set of equations. In general, the behaviour of a dynamical system can be described to a large extent by its response to a pulse perturbation, and this response is called the impulse response function (IRF). In the case of a linear system, the IRF completely characterizes the dynamics of the system, and the response to a general perturbation can be expressed by the time convolution of the IRF with the general perturbation (Wigley, 1991). In the context of emission metrics, IRFs are used in two ways. Firstly, they are used to characterize the atmospheric concentration of a given species following a pulse emission. Most species will show a single exponential decay, but the atmospheric CO_2 concentration following a pulse emission is more complex (Joos et al., 2013). Secondly, IRFs are also used to characterize the global temperature change induced by a pulse radiative forcing (Hasselmann et al., 1993; Sausen and Schumann, 2000). If one additionally linearizes the expression for the radiative forcing to obtain the radiative efficiency (Aamaas et al., 2013), one obtains a simple and useful description of the atmospheric response to the emissions of radiatively active species through a simple combination of the radiative efficiency and IRFs.

By using IRFs in the expression of emission metrics, the climate impact is explicitly decoupled into three independent parts: (i) the additional radiative forcing for a marginal increase in burden (radiative efficiency); (ii) the impact of an emission on the atmospheric burden; and, (iii) the impact of radiative forcing on the global-mean temperature for temperature-based metrics. In a coupled system, temperature changes (which might be caused by a CO_2 perturbation) will modify the absorption of CO_2 in the ocean directly due to the temperature dependency of the CO_2 solubility, but also by changes in the ocean circulation patterns, and by the biosphere, directly through increased respiration and photosynthesis or indirectly by changing precipitation (Joos et al., 1996; Friedlingstein et al., 2006; Archer et al., 2009). Many of these processes are non-linear and path dependent, and thus the IRFs are only valid for specific conditions, such as temperature (determining the CO_2 solubility in the ocean) or reference tracer concentration. In addition, the radiative efficiency of a specific species might also depend on its concentration and on the concentration of species with which there might be a spectral overlap (Tanaka et al., 2009; Gillett and Matthews, 2010; Reisinger et al., 2011). In non-linear systems (for example increased photosynthesis by higher atmospheric CO_2 concentrations – fertilization effect), the IRF will be influenced by the size and timing of the pulse (Hooss et al., 2001; Eby et al., 2009; Joos et al., 2013).

In principle, every system behaves linearly for small perturbations, and as metrics are defined as a tool to compare the impact of small emission changes (1 kg), there is a strong interest in this linear domain. Below a certain threshold, the behaviour of the IRFs will be rather independent of the size of the pulse. For CO_2 pulse sizes below 100 Gt[C], the IRF is found to be linear, but the IRF still depends on the timing and the emissions pathway (Joos et al., 2013). The non-linearities caused by the timing and pathway of emissions partially cancel (Caldeira and Kasting, 1993), though regular updates of IRFs are needed (Reisinger et al., 2011; Joos et al., 2013).

IRFs are nevertheless useful and efficient means to describe the behaviour of more complex systems (or models). They allow fast and sufficiently robust metric calculations, and give the possibility to efficiently estimate the impact of many different scenarios, as long as one remains in a linear regime. In recent times, the GWP and GTP have used a CO_2 IRF (IRF_{CO_2}) based on an updated version of the Bern coupled climate–carbon cycle model (CC-model) described in Plattner et al. (2008, Bern2.5CC), and the temperature IRF (IRF_T) from Boucher and Reddy (2008) based on a simulation with the UKMO-HadCM3 atmosphere–ocean general circulation model (AOGCM). As these IRFs are based on the behaviour of only one parent model, one should regard their application with care as they may be outliers. It is thus relevant to assess how IRFs (and consequently metric values) can differ among models. In recent years, many idealized simulations with CC-models and AOGCMs have become available in intercomparison exercises, which can be used to derive IRF_{CO_2} or IRF_T. The behaviour of these models differs considerably, and one of the aims of this study is to investigate how this is translated into variations in the IRFs. We will also use these derived IRFs to calculate GWP, GTP, and iGTP values, and quantify how they are influenced by variation in the IRFs.

This work builds on former work where IRF_T is estimated based on AOGCM simulations performed within the CMIP3 project (Olivié et al., 2012). Here, we extend the estimation of IRF_T to CMIP5 data (Taylor et al., 2012), and use the method additionally to estimate IRF_{CO_2} from recent intercomparison exercises (C^4MIP, Friedlingstein et al., 2006; LTMIP, Archer et al., 2009, and Joos et al., 2013). Due to the considerable number of models participating, we can enlighten the variation of IRFs among models, and estimate the impact of variation in IRF_{CO_2} and IRF_T on metric values. Uncertainties in the lifetime of the non-CO_2 species and in the radiative efficiencies are not considered here, but have been explored elsewhere (Wuebbles et al., 1995; Reisinger et al., 2010; Prather et al., 2012). One must also be aware that spread in IRFs based on a model intercomparison does

not necessarily represents the scientific uncertainty (Knutti, 2010; Reisinger et al., 2010). Our work is comparable with Reisinger et al. (2010), who presented uncertainty estimates for emission metrics of CO_2 and CH_4 using a simple climate model calibrated on CMIP3 AOGCM results and C^4MIP CC-model results (partially using results from OCMIP2). With respect to their study, we study more species (black carbon (BC), methane (CH_4), nitrous oxide (N_2O) and sulfur hexafluoride (SF_6)), and use data from more intercomparison exercises (LTMIP, CMIP5, and Joos et al., 2013).

The structure of the paper is as follows. In Sect. 2, we describe emission metrics and IRFs. In Sect. 3, we describe the data and method we use to derive IRFs. In Sect. 4, we present the derived IRFs, and the impact of variation in IRFs on emission metrics. In Sect. 5, we present our conclusions.

2 Emission metrics and IRFs

2.1 IRFs

In the context of emission metrics, IRFs are used as a condensed way to describe the evolution of the atmospheric burden of species after their emission, or the evolution of the global-mean temperature in response to a radiative forcing.

2.1.1 Burden IRFs

The evolution of the atmospheric burden after the pulse emission of 1 kg of a species X is often written as a sum of decaying exponential functions (modes),

$$\mathrm{IRF}_X(t) = \sum_{i=0}^{n-1} a_i \exp\frac{-t}{\tau_i}, \quad (1)$$

with

$$\sum_{i=0}^{n-1} a_i = 1. \quad (2)$$

The atmospheric burden $B_X(t)$ in response to any emission scenario $E_X(t)$ can be written as the convolution integral

$$B_X(t) = (E_X \otimes \mathrm{IRF}_X)(t) \equiv \int_{-\infty}^{t} E_X(t')\,\mathrm{IRF}_X(t-t')\,\mathrm{d}t'. \quad (3)$$

For most species one usually limits the expression to one mode, where the unique τ in Eq. (1) represents the perturbation lifetime of the species (Prather, 2007). In this study, we consider species with a wide range of lifetimes to capture the different dynamics: BC, CH_4, N_2O, and SF_6. BC has a lifetime of around a week, but it may vary depending on the location and timing of the emissions, while CH_4, N_2O, and SF_6 have more stable lifetimes of around 12, 114, and 3200 yr, respectively (see Table 1).

We take into account the impact of CH_4 and N_2O on their own lifetimes (Seinfeld and Pandis, 2006; Prather, 2007). Emissions of CH_4 also lead to the formation of tropospheric ozone and stratospheric water vapour (their radiative impact is included in the radiative efficiency of CH_4). The radiative forcing from CO_2 produced in the oxidation of CH_4 is not taken into account, as this CO_2 is often already accounted for in the CO_2 emission inventories (for its impact, see Boucher et al., 2009). One should also be aware of the fact that tropospheric OH concentrations which determine the loss rate of CH_4 are estimated to have uncertainties of around $\pm 15\,\%$ (Reisinger et al., 2011).

The perturbation lifetime of CO_2 is more complex. A part of a pulse emission disappears rapidly from the atmosphere on a timescale of 1 to 10 yr, while a substantial part remains in the atmosphere for a much longer time (Archer et al., 1997, 2009). One mode is insufficient to describe the atmospheric CO_2 burden evolution after a pulse emission (Joos et al., 1996; Forster et al., 2007; Archer et al., 2009). A satisfactory description for the evolution of CO_2 used in Forster et al. (2007) is an expression with four modes ($n = 4$ in Eq. 1), and the corresponding values of a_i and τ_i are given in the upper row of Table 3. Notice that $\tau_0 = \infty$, indicating that 21.7 % of the emission is assumed to stay perpetually in the atmosphere ($a_0 = 0.217$).

If one additionally assumes that the RF is a linear function of the atmospheric burden, then the evolution of the RF as a function of time can be expressed by a simple multiplication of the radiative efficiency and the IRF (Aamaas et al., 2013). In general linearity does not hold for CO_2, CH_4, or N_2O where the RF shows a non-linear dependence on their burden – moreover N_2O and CH_4 have a spectral overlap (Ramaswamy et al., 2001, Table 6.2). However, a linear approximation can be used when assuming a marginal perturbation around a well-defined reference state. Approximate values for the radiative efficiency of different species are given in Table 1. The radiative efficiency of CO_2 (see Table 1) is based on the radiative forcing expression for CO_2 in Ramaswamy et al. (2001, Table 6.2), assuming a background mixing ratio of 378 ppm (Forster et al., 2007, Sect. 2.10.2 and Table 2.14).

2.1.2 Temperature IRF

IRFs are also used to express the temperature evolution in response to a specified radiative forcing. The expected global-mean temperature change, $T(t)$, due to a radiative forcing can be approximately described by a convolution integral of the radiative forcing, $\mathrm{RF}(t)$, with the temperature IRF, $\mathrm{IRF}_T(t)$:

$$T(t) = (\mathrm{RF} \otimes \mathrm{IRF}_T)(t) \equiv \int_{-\infty}^{t} \mathrm{RF}(t')\,\mathrm{IRF}_T(t-t')\,\mathrm{d}t'. \quad (4)$$

Table 1. Lifetime and radiative efficiency of BC, CH_4, CO_2, N_2O, and SF_6 (see Forster et al., 2007, and Fuglestvedt et al., 2010). For the lifetime of CO_2, see Table 3.

		BC	CH_4	CO_2	N_2O	SF_6
τ	(yr)	0.02	12	–	114	3200
A_X	($W\,m^{-2}\,kg^{-1}$)	1.96×10^{-9}	1.82×10^{-13}	1.81×10^{-15}	3.88×10^{-13}	2.00×10^{-11}

The IRF_T is often described as a sum of decaying exponential functions,

$$IRF_T(t) = \sum_{i=1}^{n} \frac{f_i}{\tau_i} \exp \frac{-t}{\tau_i}. \quad (5)$$

This function describes the evolution of the global-mean temperature change after a δ-pulse radiative forcing (the integrated amount of forcing from a δ-pulse imposed on the system is comparable to a forcing of $1\,W\,m^{-2}$ during 1 yr). For a RF step scenario that jumps at $t = 0$ from 0 to $1\,W\,m^{-2}$ and remains constant at that value for $t > 0$, one finds, using Eqs. (4) and (5), that the temperature evolution $T(t)$ can be written as

$$T(t) = \sum_{i=1}^{n} f_i \left(1 - \exp \frac{-t}{\tau_i}\right). \quad (6)$$

This shows that the sum of the f_i in IRF_T can be interpreted as the climate sensitivity, i.e. $\lambda = \sum_{i=1}^{n} f_i$ (taking $t \rightarrow \infty$ in Eq. 6). The climate sensitivity is here defined as the change in equilibrium global-mean temperature per unit forcing (Hansen et al., 2005; Hansen and Sato, 2012).

In the literature, one finds IRF_T expressions with $n = 1$ (Hasselmann et al., 1993; Shine et al., 2005), $n = 2$ (Hooss et al., 2001; Boucher and Reddy, 2008), and $n = 3$ (Li and Jarvis, 2009). Using two time constants describes the AOGCM temperature evolution response to a RF reasonably well (Boucher and Reddy, 2008; Li and Jarvis, 2009; Olivié and Stuber, 2010; Olivié et al., 2012), while one time constant is inadequate for most applications (Shine et al., 2005; Gillett and Matthews, 2010; Olivié et al., 2012). A frequently used expression with $n = 2$ is the one presented in Boucher and Reddy (2008), and the corresponding values of f_i and τ_i are given in the upper row of Table 4. For expressions with $n \geq 2$, the first mode represents the fast response of the atmosphere, the land surface, and the ocean mixed layer, while the other modes represent the slow response of the deep ocean.

2.2 Emission metrics

Emission metrics are a useful tool to efficiently quantify and compare the impact of the emissions of different species. While emission metrics can also be calculated using more complex models (Wuebbles et al., 1995; Tanaka et al., 2009, 2010; Reisinger et al., 2010; Gillett and Matthews, 2010), we use the IRF approach as described above due to its efficiency, repeatability, and utility in a wide range of applications.

The absolute global warming potential (AGWP) of a species is the time-integrated RF caused by the emission of 1 kg of that species,

$$AGWP_X(H) = \int_0^H A_X\, IRF_X(t)\, dt, \quad (7)$$

with H the time horizon, $IRF_X(t)$ the burden IRF (see Eq. 1), and A_X the radiative efficiency of species X. The radiative efficiency can depend on the background concentration, but we assume a constant background as is common for emission metrics (Joos et al., 2013; Aamaas et al., 2013). The radiative efficiency values we use are given in Table 1. The dimensionless GWP of a species is the AGWP of that species divided by the AGWP of CO_2,

$$GWP_X(H) = \frac{AGWP_X(H)}{AGWP_{CO_2}(H)}. \quad (8)$$

The GWP metric has been used extensively over the last two decades to compare the climate effect of various species.

By combining the burden IRF and the temperature IRF, one can express the global-mean temperature response due to the emission of a species. The absolute global temperature change potential (AGTP) indicates the impact of the emission of 1 kg of a certain species on the global-mean temperature at a certain time,

$$AGTP_X(H) = \int_0^H A_X\, IRF_X(t)\, IRF_T(H - t)\, dt, \quad (9)$$

with $IRF_T(t)$ the temperature IRF (see Eq. 5). The dimensionless GTP of a species is the AGTP of that species divided by the AGTP of CO_2,

$$GTP_X(H) = \frac{AGTP_X(H)}{AGTP_{CO_2}(H)}. \quad (10)$$

The integrated absolute temperature change potential (iAGTP) is the time integral of AGTP,

$$iAGTP_X(H) = \int_0^H AGTP_X(t)\, dt. \quad (11)$$

The dimensionless iGTP of a species is the iAGTP of that species divided by the iAGTP of CO_2,

$$iGTP_X(H) = \frac{iAGTP_X(H)}{iAGTP_{CO_2}(H)}. \quad (12)$$

3 Method and data

To obtain estimates for IRF_{CO_2} and IRF_T, we use results from more complex models. As we are interested in possible uncertainties in emission metrics, we focus on data from intercomparison exercises with different models participating in the same experimental setup.

3.1 Data

Here we describe the data used to derive the IRFs. We will also shortly describe the data on which the reference IRF_{CO_2} (Forster et al., 2007) and IRF_T (Boucher and Reddy, 2008) are based. An overview of some of the characteristics of the intercomparison exercises can be found in Table 2.

3.1.1 Forster et al. (2007)

The IRF_{CO_2} which has been used in Forster et al. (2007), is based on a 1000 yr-long simulation with the Bern CC-model (Plattner et al., 2008, Bern2.5CC). In that simulation, a background CO_2 mixing ratio of 378 ppm and a pulse emission of 40 Gt[C] were used. We will refer to this data set and IRF_{CO_2} derived from it as J07.

3.1.2 C^4MIP

The C^4MIP (Coupled Climate–Carbon Cycle Model Intercomparison Project) experiments have been performed simulating the 1860–2100 period with CC-models (Friedlingstein et al., 2006). For the anthropogenic CO_2 emissions, estimates based on observed concentrations have been used up to around year 2000 and SRES scenario A2 values for the 21st century (Nakicenovic et al., 2000). The annual emissions increase from $\sim 1\,\mathrm{Gt[C]\,yr^{-1}}$ in 1900, to $\sim 8\,\mathrm{Gt[C]\,yr^{-1}}$ in 2000, and $\sim 30\,\mathrm{Gt[C]\,yr^{-1}}$ in 2100.

Eleven CC-models participated in this intercomparison exercise, of which 7 are AOGCMs and 4 are models of intermediate complexity. These models are BERN-CC, CSM-1, CLIMBER2-LPJ, FRCGC, HadCM3LC, IPSL-CM2C, LLNL, IPSL-CM4-LOOP, MPI, UMD, and Uvic-2.7. A short description of these models can be found in Friedlingstein et al. (2006). Two different experiments were performed. In an uncoupled experiment (u) temperature feedbacks on the carbon cycle were not included, while in the coupled experiment (c) temperature feedbacks were included. All models indicated that a larger fraction of anthropogenic CO_2 stays airborne if temperature feedbacks are included.

3.1.3 LTMIP

A second data set we use to derive IRF_{CO_2} is LTMIP (Long Tail Model Intercomparison Project) (Archer et al., 2009). The aim of this project was to quantify the long-term fate of fossil fuel CO_2 emissions in the atmosphere, ocean, and terrestrial biosphere. The participating groups performed 10^4 yr-long simulations with CC-models, emitting CO_2 pulses of 1000 Gt[C] and 5000 Gt[C]. The reference state was an atmospheric mixing ratio of 286 ppm CO_2.

Different simulations have been performed, differing by the feedbacks taken into account in the CC-models. We have used the results from the reference simulation with a 1000 Gt[C] pulse emission and no feedbacks – this is a simulation performed by most of the models. These models are CC_SED, CLIMBER-2, GENIE8, GENIE16, GEOCYC, LTCM, MESMO, MPI-UW, and UVIC-2.8. A short description of these models can be found in Archer et al. (2009) and Cao et al. (2009). With one of these models (UVIC-2.8), Eby et al. (2009) further illustrate that the time required to absorb anthropogenic CO_2 strongly depends on the total emission amount.

3.1.4 Joos et al. (2013)

The recent study of Joos et al. (2013) estimated IRF_{CO_2} with current state-of-the-art CC-models. They performed simulations with a length of 1000 yr and an emission pulse of 100 Gt[C]. The reference state was an atmospheric mixing ratio of 389 ppm CO_2. The 15 models of which we used data are ACC2, Bern2.5D-LPJ, Bern3D-LPJ, Bern-SAR, CLIMBER-2-LPJmL, DCESS, GENIE, HadGEM2-ES, LOVECLIM1.1, MAGICC6, MESMO1.00, MPI-ESM, NCAR CSM1.4, TOTEM, and UVic2.9. We will refer to this data set as J13. Joos et al. (2013) additionally studied the impact of a CO_2 pulse emission on the global-mean temperature, sea level, and ocean heat content, and performed a variety of sensitivity studies.

3.1.5 Boucher and Reddy (2008)

Boucher and Reddy (2008) present an IRF_T, derived from a 1000 yr-long simulation with the UKMO-HadCM3 AOGCM. In this simulation the RF was modified by increasing the CO_2 concentration by $2\,\%\,\mathrm{yr^{-1}}$ up to a quadrupling (reached after 70 yr), after which the CO_2 concentration was kept constant. The IRF_T of Boucher and Reddy (2008) contains two modes, with time constants of 8.4 and 409.5 yr. The values of f_i and τ_i can also be found in the top row of Table 4. Li and Jarvis (2009) used the same data but a different method to estimate the modes. Using two modes they find very similar values, and using three modes small differences in the integrated IRF_T only show up after 500 yr.

3.1.6 CMIP3

The first set of AOGCM results we use to derive IRF_T is taken from the World Climate Research Programme's Coupled Model Intercomparison Project phase 3 (CMIP3), which has been used for the IPCC Fourth Assessment Report (Solomon et al., 2007). Among the different simulations available from the CMIP3 exercise, we use the

Table 2. Overview of the different data sets used to derive IRF_{CO_2} and IRF_T. The number of models used here might be lower than the number of models participating in the intercomparison exercise.

	Experimental setup	Length (yr)	Models (#)	Release	Reference
J07	Pulse CO_2 emission	1000	1	2007	Forster et al. (2007)
C^4MIP	Gradual CO_2 emission (SRES A2)	140 (240)	11	2006	Friedlingstein et al. (2006)
LTMIP	Pulse CO_2 emission	10 000	9	2009	Archer et al. (2009)
J13	Pulse CO_2 emission	1000	15	2013	Joos et al. (2013)
BR08	Linear RF increase + stabilization	1000	1	2008	Boucher and Reddy (2008)
CMIP3	Linear RF increase + stabilization	70–300	15	2006	Randall et al. (2007)
CMIP5	Step RF increase/linear RF increase	140–150	15	2011	Taylor et al. (2012)

Table 3. Estimates of the parameters in IRF_{CO_2}: J07 is the IRF_{CO_2} used in Forster et al. (2007), and C^4MIP(u), C^4MIP(c), and LTMIP are the IRF_{CO_2} derived using the corresponding data sets. C^4MIP(c) represents an experiment with a temperature feedback, and C^4MIP(u) without. J13* refers to the coefficients as derived and published in Joos et al. (2013). In all the IRF_{CO_2} is $\tau_0 = \infty$. The median, and 5- and 95-percentile values are indicated.

	τ_1 (yr)	τ_2 (yr)	τ_3 (yr)	a_0	a_1	a_2	a_3
J07	172.9	18.51	1.19	0.217	0.259	0.338	0.186
C^4MIP(u)	$177.56 \pm 23\%$	$11.94 \pm 26\%$	$1.10 \pm 7\%$	$0.19 \pm 13\%$	$0.16 \pm 34\%$	$0.36 \pm 31\%$	$0.29 \pm 37\%$
C^4MIP(c)	$186.88 \pm 23\%$	$13.13 \pm 27\%$	$1.11 \pm 8\%$	$0.21 \pm 10\%$	$0.19 \pm 33\%$	$0.34 \pm 30\%$	$0.26 \pm 38\%$
LTMIP	$270.59 \pm 38\%$	$33.70 \pm 111\%$	$1.65 \pm 36\%$	$0.20 \pm 11\%$	$0.50 \pm 26\%$	$0.22 \pm 36\%$	$0.08 \pm 153\%$
J13	$239.60 \pm 58\%$	$18.42 \pm 68\%$	$1.64 \pm 63\%$	$0.23 \pm 20\%$	$0.28 \pm 33\%$	$0.35 \pm 28\%$	$0.14 \pm 30\%$
J13*	394.4	36.54	4.30	0.217	0.224	0.282	0.276

idealized experiments where the CO_2 concentration increases by $1\,\%\,yr^{-1}$, and is kept constant after 70 yr (doubling of CO_2) or after 140 yr (quadrupling of CO_2). These are gradually changing scenarios, and have for most of the AOGCMs a length of 210–290 yr, but less than 100 yr for a few of them. The subset of 15 models we use consists of CGCM3.1(T47), CNRM-CM3, ECHO-G, FGOALS-g1.0, GFDL-CM2.0, GFDL-CM2.1, GISS-EH, GISS-ER, INM-CM3.0, IPSL-CM4, MIROC3.2(hires), MIROC3.2(medres), MRI-CGCM2.3.2, UKMO-HadCM3, and UKMO-HadGEM1. More information on these models can be found in Randall et al. (2007).

For the models used in this intercomparison exercise (except for CNRM-CM3), also the climate sensitivity λ (see Sect. 2.1.2) has been estimated in Randall et al. (2007, Table 8.2) based on an experiment where the atmosphere general circulation models alone were coupled to a mixed layer ocean model (Solomon et al., 2007). In one of the approaches we use the estimated climate sensitivity as an additional constraint, and we refer to that case as CMIP3*.

3.1.7 CMIP5

From the more recent CMIP5 exercise (Taylor et al., 2012), we use the scenario with an instantaneous quadrupling of the CO_2 concentration, and the one with a gradual increase in CO_2 concentration at a rate of $1\,\%\,yr^{-1}$ (without stabilization). The length of the simulations is 140–150 yr, which is considerably shorter than the experiments in CMIP3. We use the results from 15 models, i.e. CanESM2, CNRM-CM5, CSIRO-Mk3.6.0, GFDL-CM3, GFDL-ESM2G, GFDL-ESM2M, HadGEM2-ES, INM-CM4, IPSL-CM5A-LR, MIROC5, MIROC-ESM, MPI-ESM-LR, MPI-ESM-P, MRI-CGCM3, and NorESM1-M.

3.2 Method

In this section, we explain how we estimate the parameters in the IRFs, how we construct the IRF distributions, and how we calculate the spread in the emission metrics.

3.2.1 Estimating the IRF parameters

For every CC-model and AOGCM in the data sets above, we have estimated the parameters in the IRFs of Eqs. (1) and (5), respectively. We choose to use four modes ($n = 4$) in IRF_{CO_2} (one of which is a constant term as we take $\tau_0 = \infty$) (Joos et al., 1996, 2013; Forster et al., 2007), and two modes ($n = 2$) in IRF_T (Boucher and Reddy, 2008; Li and Jarvis, 2009; Olivié et al., 2012). To find the parameter values in the IRFs that best fit the behaviour of one single CC-model

Table 4. Estimates of the parameters in IRF_T: BR08 is the IRF_T used in Boucher and Reddy (2008), and CMIP3, CMIP3*, and CMIP5 are the IRF_T derived using CMIP3 and CMIP5 data. The CMIP3 IRF_T is based on AOGCM experiments alone, while the CMIP3* IRF_T additionally includes the independently estimated climate sensitivities. The median, and 5- and 95-percentile values are indicated.

	τ_1 (yr)	τ_2 (yr)	f_1 ($K\,W^{-1}\,m^2$)	f_2 ($K\,W^{-1}\,m^2$)
BR08	8.4	409.5	0.631	0.429
CMIP3	$7.15 \pm 35\,\%$	$105.55 \pm 38\,\%$	$0.48 \pm 30\,\%$	$0.20 \pm 52\,\%$
CMIP3*	$7.24 \pm 43\,\%$	$244.44 \pm 130\,\%$	$0.49 \pm 25\,\%$	$0.36 \pm 91\,\%$
CMIP5	$2.57 \pm 46\,\%$	$82.24 \pm 192\,\%$	$0.43 \pm 29\,\%$	$0.32 \pm 59\,\%$

or AOGCM, we use probabilistic inverse estimation theory (Tarantola, 2005, p. 69), applied for simple climate models in Tanaka et al. (2009) and Olivié and Stuber (2010). It has been recently used on CMIP3 data (Olivié et al., 2012) to derive IRF_T, and here we apply it to derive both IRF_{CO_2} and IRF_T. We use it to optimize the value of the IRF_{CO_2} (IRF_T) parameters by minimising the difference between the time evolution of the CO_2 concentration (temperature) in the CC-model (AOGCM) and the CO_2 concentration (temperature) obtained from the convolution of the CO_2 emission (radiative forcing) scenario with the IRF_{CO_2} (IRF_T), but also taking into account how much the IRF parameters deviate from a priori values (Tarantola, 2005, Eq. 3.46).

For the parameters in IRF_{CO_2}, the a priori values are the J07 values (see Table 3), and for IRF_T we have chosen $0.2\,K\,W^{-1}\,m^2$, $0.5\,K\,W^{-1}\,m^2$, 10 yr, and 100 yr as a priori values for f_1, f_2, τ_1, and τ_2, respectively. It has been assumed that there was no a priori correlation among the parameters of each IRF, and no correlation between the CC-model or AOGCM data for different years. To implement the condition that $\sum_{i=0}^{3} a_i = 1$ in IRF_{CO_2}, we introduce three parameters b_i which are related to the four a_i by

$$a_0 = \frac{1}{1+\sum_{j=1}^{3} b_j} \tag{13}$$

and

$$a_i = \frac{b_i}{1+\sum_{j=1}^{3} b_j} (i = 1,2,3)\,, \tag{14}$$

where $0 < b_i < \infty$ $(i = 1,2,3)$ are now the parameters which have to be estimated. We assume that all parameters (b_i, f_i, and τ_i) have a log-normal distribution, which guarantees that they remain positive. So for every single CC-model or AOGCM, we find a corresponding set of parameters which best reproduces its behaviour. In the CMIP3* approach, we impose the value of the climate sensitivity λ (Randall et al., 2007, Table 8.2) by eliminating the variable f_2 and replacing it by $\lambda - f_1$.

In principle, one can imagine a variety of numerical experiments with CC-models and AOGCMs, differing in the time evolution of the CO_2 emission $E_{CO_2}(t)$ and the radiative forcing $RF(t)$, respectively. Deriving an IRF from an experiment can be more or less difficult depending on the type of scenario. Ideal are experiments where the response of the CC-model or AOGCMs gives directly an IRF. This can be easily realized for CC-models when using a pulse emission, as in J07, LTMIP, and J13. However, for the temperature experiments, a δ-pulse experiment is difficult to realize, and therefore a step in the radiative forcing which is kept constant or decays exponentially is more common (Olivié and Stuber, 2010). For experiments not based on pulses, deriving the IRF can be more complicated, and one must be aware that the IRF might be poorly constrained.

3.2.2 IRF distribution

Once all the IRF parameter sets are found, where each set best reproduces the behaviour of one CC-model or AOGCM, we group them together per intercomparison exercise and derive a multivariate distribution for the parameters of the IRF – the distribution assumes that the logarithm of the parameters are normally distributed. This gives four IRF_{CO_2} distributions based on C^4MIP(u), C^4MIP(c), LTMIP, and J13 data, and three IRF_T distributions based on CMIP3, CMIP3*, and CMIP5. When $\boldsymbol{x}$ is the vector consisting of the logarithm of the parameters of the IRF_{CO_2},

$$\boldsymbol{x} = (\log\tau_1, \log\tau_2, \log\tau_3, \log b_1, \log b_2, \log b_3)\,, \tag{15}$$

then the distribution of the parameters in the IRF_{CO_2} can be expressed as

$$P(\boldsymbol{X} = \boldsymbol{x}) \sim \exp\left(-\frac{1}{2}(\boldsymbol{x}-\bar{\boldsymbol{x}})^T\,\boldsymbol{\Sigma}^{-1}(\boldsymbol{x}-\bar{\boldsymbol{x}})\right), \tag{16}$$

where

$$\bar{\boldsymbol{x}} = \frac{1}{m}\sum_{i=1}^{m} \boldsymbol{x}_i \tag{17}$$

and

$$\boldsymbol{\Sigma} = \frac{1}{m-1}\sum_{i=1}^{m} (\boldsymbol{x}_i - \bar{\boldsymbol{x}})^T (\boldsymbol{x}_i - \bar{\boldsymbol{x}})\,. \tag{18}$$

The vector $\bar{\boldsymbol{x}}$ and the matrix $\boldsymbol{\Sigma}$ are estimates of the mean vector and the covariance matrix, respectively, and the index i runs over all models in the specific intercomparison exercise (for m, see Table 2).

In case of the IRF_T distribution, the Eqs. (16–18) remain valid, but the vector $\boldsymbol{x}$ now represents the parameters in IRF_T, i.e.

$$\boldsymbol{x} = (\log \tau_1, \log \tau_2, \log f_1, \log f_2)\,. \quad (19)$$

3.2.3 Monte Carlo simulation

To obtain the distribution of the GWP, GTP, and iGTP metrics, we perform Monte Carlo simulations (2×10^4 members) using the derived IRF distributions. To obtain the GTP and iGTP distribution, one uses both IRF_{CO_2} and IRF_T, and for simplicity, we assume that there is no correlation between the IRF_{CO_2} and IRF_T parameter values.

Performing Monte Carlo simulations using multivariate distributions (as in the IRFs) necessitates the factorization of the covariance matrix $\boldsymbol{\Sigma}$ as $\boldsymbol{\Sigma} = \mathbf{L}\,\mathbf{L}^T$, where $\mathbf{L}$ is a lower triangular matrix. Applying this matrix $\mathbf{L}$ to a vector $\boldsymbol{y}$ of uncorrelated normally distributed values generates a vector $\boldsymbol{x} = \mathbf{L}\,\boldsymbol{y}$ with the covariance properties of the system being modelled.

4 Results

In this section we first describe the IRF distributions obtained by fitting the CC-model and AOGCM results. Then we present the GWP, GTP, and iGTP emission metric values we obtain for time horizons between 20 and 500 yr for BC, CH_4, N_2O, and SF_6. These species are chosen as they span a wide range of lifetimes, i.e. 1 week, 12, 114, and 3200 yr, respectively.

4.1 IRFs

4.1.1 CO_2 IRF

Figure 1 shows the principal results for IRF_{CO_2}. Figure 1a shows IRF_{CO_2} for the reference J07 (black), and for the four distributions C^4MIP(u) (red), C^4MIP(c) (blue), LTMIP (green), and J13 (purple) derived from the respective intercomparison exercises (full lines indicate the median value, dashed lines the 5- and 95-percentile values).

We estimated the J13 IRF_{CO_2} based on the original data, independent from the estimation presented in Joos et al. (2013). The median of J13 lies very close to the J07 reference. Our 5- and 95-percentile values of 0.47–0.71, 0.33–0.50, and 0.18–0.30 at $H = 20$, 100, and 1000 yr, respectively, agree well with the values obtained in Joos et al. (2013). Converting the mean and 2σ values of Joos et al. (2013, Sect. 4.1) into 5- and 95-percentile values gives 0.49–0.71, 0.30–0.52, and 0.18–0.32 at $H = 20$, 100, and 1000 yr, respectively. The experimental setup in J13 is most suited for deriving IRF_{CO_2}: the behaviour of the CC-models stays in the linear regime, and deriving the IRF_{CO_2} is reduced to finding the coefficients which best describe the obtained IRF_{CO_2} curve.

The IRF_{CO_2} based on LTMIP is significantly higher than the standard J07; almost 95 % of its distribution is higher than J07. However, the estimate of the long-term value around year 1000 in LTMIP is again similar to the J07 value. The large differences for earlier times are caused by the very large emission size, i.e. 1000 Gt[C]. This large pulse size introduces non-linearities (Joos et al., 2013), as the ocean mixed layer is easily saturated inhibiting a faster take up of atmospheric CO_2. The fact that the LTMIP experiments were in the non-linear regime makes the derived IRF_{CO_2} less suitable to be used in metric calculations (where one tries to incorporate the effect of small emission amounts).

The two IRF_{CO_2} based on C^4MIP give results slightly lower than J07 and J13, and considerably lower than LTMIP. To guarantee that the CC-models were still in the linear regime, we have used data only up to year 2000 (see Appendix A). For all models in C^4MIP(u), the CO_2 concentration falls in the range 344–392, 397–465, and 475–570 ppm for the years 2000, 2025, and 2050, respectively, and in 347–401, 400–483, and 489–604 ppm in C^4MIP(c). This limits the length of the time series used to derive the IRF_{CO_2} to approximately 140 yr, which is considerably shorter than in J13 or LTMIP. In addition, the near-exponential increase in CO_2 emissions in this experiment might complicate the estimation of IRF_{CO_2}. In the case of an exact exponential emission scenario, quite different IRF_{CO_2} can lead to exactly the same evolution of the CO_2 burden (see Eq. 3). This implies that if more than one mode must be estimated in the IRF_{CO_2}, their weights and timescales can become indeterminate (see Appendix B). However, as the emission scenario here is not exactly exponential, the experiment still contains additional information (Gloor et al., 2010).

One can also see that the results from the coupled experiment (c) give larger values for IRF_{CO_2}; the increasing temperature in that experiment decreases the net CO_2 uptake, leaving a larger fraction of CO_2 in the atmosphere. At 100 yr after the emission, a fraction of 0.31 is still in the atmosphere in C^4MIP(c), while it is only 0.28 in C^4MIP(u). Joos et al. (2013, Fig. 7) show the impact of the temperature feedback for one model (Bern3D-LPJ) on IRF_{CO_2}; for an emission pulse of 100 Gt[C] they find differences around 15–20 % at 100 yr after the emission.

The spread in J13 is slightly smaller than in LTMIP, but for LTMIP the spread becomes again smaller at the end of the shown horizon range. Both C^4MIP IRF_{CO_2} show spreads comparable with the spread in J13. The 5- and 95-percentile values at $H = 100$ yr are 0.39–0.69 for LTMIP, 0.21–0.37 for C^4MIP(u), 0.24–0.40 for C^4MIP(c), and 0.33–0.50 for J13.

Figure 1b shows the time-integrated IRF_{CO_2} for the reference J07, and for the four distributions C^4MIP(u), C^4MIP(c), LTMIP, and J13. J13 and LTMIP show slightly higher values than J07 (10 % for J13 and 20 % for LTMIP), but a similar temporal evolution. C^4MIP(u) and C^4MIP(c) give slightly lower values, in accordance with the lower IRF_{CO_2}.

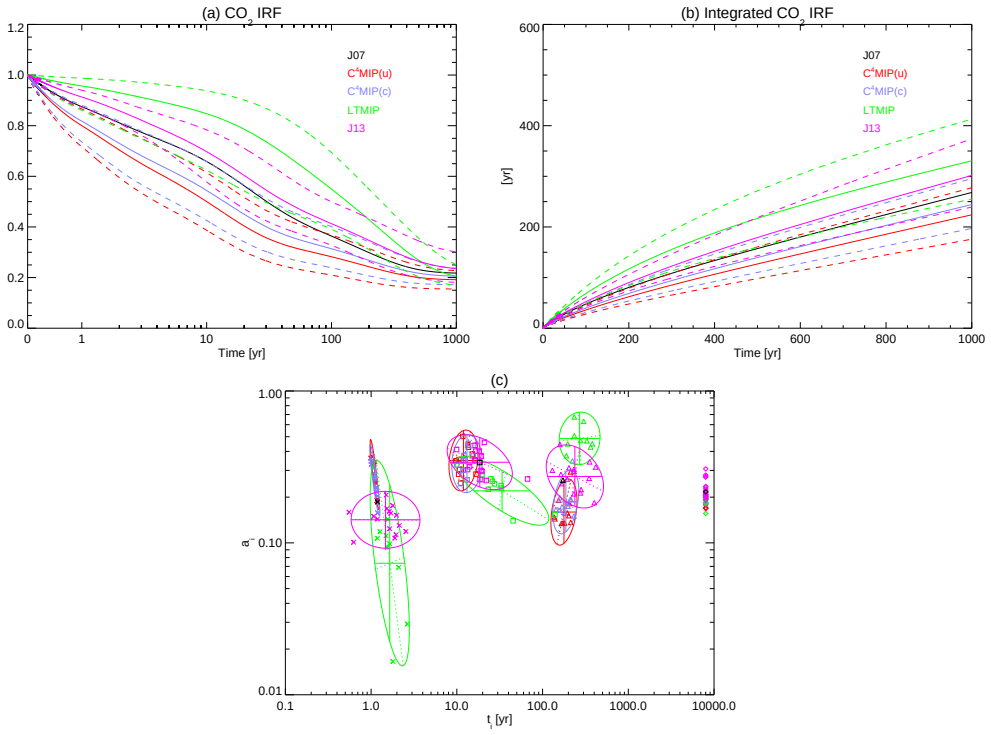

Fig. 1. Overview of five different $\mathrm{IRF}_{\mathrm{CO}_2}$ distributions: J07 (black), C^{4}MIP(u) (red), C^{4}MIP(c) (blue), LTMIP (green), and J13 (purple). **(a)** $\mathrm{IRF}_{\mathrm{CO}_2}$ as in Eq. (1) with median (full line) and 5- and 95-percentile values (dashed lines) indicated. The horizontal axis is linear from 0 to 1 yr, and logarithmic from 1 to 1000 yr. The vertical axis is dimensionless. **(b)** Integrated $\mathrm{IRF}_{\mathrm{CO}_2}$. The horizontal axis is linear. **(c)** Estimates for the parameters in $\mathrm{IRF}_{\mathrm{CO}_2}$. Every single dot corresponds with one of the four modes, i.e. (τ_0, a_0) (diamond), (τ_1, a_1) (triangle), (τ_2, a_2) (square), or (τ_3, a_3) (cross). The (τ_0, a_0) tuples (which would fall off the figure as $\tau_0 = \infty$) are given at the right of the figure. The individual dots represent the best estimates for the individual CC-models, while the ellipses represent the distributions derived from the individual estimates, grouped per intercomparison exercise. Inside the ellipses falls 90 % of the distribution. The vertical axis is dimensionless.

Figure 1c shows best estimates for the parameters of the four modes in $\mathrm{IRF}_{\mathrm{CO}_2}$ when calibrated to the individual CC-models. Every single dot corresponds with a tuple (τ_i, a_i) in Eq. (1). The $\mathrm{IRF}_{\mathrm{CO}_2}$ distributions obtained by combining the results within the same intercomparison exercise are represented by the ellipses. The area in the ellipses covers 90 % of the distributions. Tilted ellipses indicate that there is a correlation between the value of τ_i and a_i. There exist also correlations between the a_i and τ_j from different modes ($i \neq j$), but they are not represented in this figure. One can see that the J13, C^{4}MIP(u), and C^{4}MIP(c) experiments give parameter values which are not very different from J07. LTMIP gives values which deviate slightly more from J07, e.g. higher values for all the time constants. Also the contribution a_1 from the century-like mode is considerably larger, while the contribution from the other modes is lower.

The values of $\bar{\boldsymbol{x}}$ and $\boldsymbol{\Sigma}$ describing the different derived $\mathrm{IRF}_{\mathrm{CO}_2}$ distributions can be found in Table 5.

4.1.2 Temperature IRF

Figure 2 shows the principal results for IRF_T. Figure 2a shows IRF_T as defined in Eq. (5). We have indicated the reference distribution from Boucher and Reddy (2008) (black), and the three distributions obtained from the intercomparison exercise data, i.e. CMIP3 (red), CMIP3* (blue) and CMIP5 (green). One can notice that the CMIP5 IRF_T is highest for the first 5 yr (the CMIP5 IRF_T starts at $0.17\,\mathrm{K\,W^{-1}\,m^2\,yr^{-1}}$, while it starts at 0.076 for BR08 and 0.069 for both CMIP3 and CMIP3*), but the CMIP5 IRF_T is lowest in the 100–1000 yr range, where it additionally shows the largest spread (in a logarithmic sense). For the period 100–1000 yr, one can further observe a considerable difference between CMIP3 and CMIP3*, and that CMIP3* is most similar to BR08; for example, at 200 yr we find for BR08, CMIP3, CMIP3*, and CMIP5 the values 6.4, 2.8, 5.5, and 3.0 ($\times\, 10^{-4}\,\mathrm{K\,W^{-1}\,m^2\,yr^{-1}}$). Though, care is needed in interpreting the results for times of 200 yr and greater as the experimental setups do not cover these time periods well.

Figure 2b shows the integrated IRF_T presented in Eq. (6). The CMIP3 and CMIP3* approach are rather similar below 100 yr, but deviate strongly later. The CMIP5 curve is considerably higher the first 10 yr due to its higher initial IRF_T, and lies between the CMIP3 and CMIP3* curves for the period after 100 yr. The asymptotic value of the integrated IRF_T

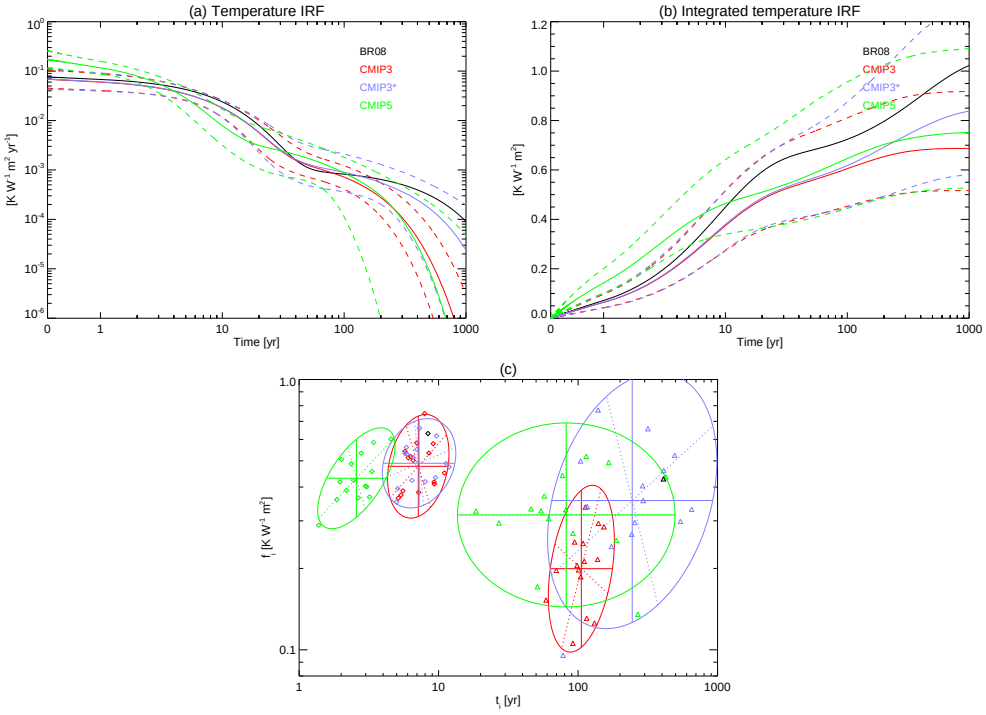

Fig. 2. Overview of four different IRF_T distributions: BR08 (black), CMIP3 (red), CMIP3* (blue), and CMIP5 (green). **(a)** IRF_T as in Eq. (5) with median (full line) and 5- and 95-percentile values (dashed lines) indicated. The horizontal axis is linear from 0 to 1 yr, and logarithmic from 1 to 1000 yr. **(b)** Integrated IRF_T as in Eq. (6). **(c)** Estimates of the parameters in IRF_T. Every single dot corresponds with one of the two modes in a separate AOGCM, i.e. the fast mode (τ_1, f_1) (diamonds) or the slow mode (τ_2, f_2) (triangles). The ellipses represent the distributions of the IRF_T parameters derived from the individual estimates, grouped per intercomparison project. Inside the ellipses falls 90 % of the distribution.

curves for $t \to \infty$ is the climate sensitivity, which is clearly highest for BR08 and CMIP3*. The climate sensitivity shows similar spreads among the IRF_T, i.e. 0.4 K for CMIP3, 0.6 K for CMIP5 and 0.7 K for CMIP3* (5–95 % spread). Again, care is needed in interpreting the climate sensitivities as they are often based on short time periods (100–200 yr).

The best estimates for the IRF_T parameters when calibrated to the individual AOGCMs are shown as separate symbols in Fig. 2c. The derived distributions are represented by the ellipses (the area within the ellipses represents 90 % of the distribution). The fast mode shows a response time of the order of 2–10 yr, and the slow mode of the order of 30–500 yr. The CMIP3* approach gives for (τ_1, f_1) results similar to CMIP3, but for (τ_2, f_2) considerably higher values, reflecting a considerably higher climate sensitivity. The CMIP5 results show relatively small values for τ_1, which is probably related to the type of experiment, i.e. an instantaneous increase in the radiative forcing (Olivié et al., 2012). The CMIP5 results also show lower values for the time constant of the slow mode τ_2, together with a relatively large spread in this parameter; this is probably related to the short length of the CMIP5 experiments

The values of $\bar{\boldsymbol{x}}$ and $\boldsymbol{\Sigma}$ describing the different derived IRF_T distributions can be found in Table 6.

4.2 Impact of variation in IRFs on metrics

Here we present metric values and their variations calculated with the IRF distributions presented above. We use the expressions from Sect. 2 and take into account that the $\mathrm{IRF}_{\mathrm{CO_2}}$ and IRF_T are themselves distributions by performing Monte Carlo simulations. Note that all parameter values such as radiative efficiencies, lifetimes of non-$\mathrm{CO_2}$ species, and coefficients of the reference $\mathrm{IRF}_{\mathrm{CO_2}}$ J07 and IRF_T BR08 are taken just as in Forster et al. (2007) and Fuglestvedt et al. (2010).

Figure 3 shows the evolution of the GWP, GTP, and iGTP metric as a function of the time horizon for all combinations of the four $\mathrm{IRF}_{\mathrm{CO_2}}$ and three IRF_T distributions for BC, $\mathrm{CH_4}$, $\mathrm{N_2O}$, and $\mathrm{SF_6}$. Every combination gives a distribution, for which only the median is indicated by a black line (how broad the metric distributions are will be shown later). Only 4 lines represent GWP, as there is no dependency on the IRF_T. The red lines are the results obtained by combining the reference IRFs J07 and BR08.

Metric values for horizons between 20 and 500 yr fall in the range 1–3000 for BC, 0.1–100 for $\mathrm{CH_4}$, 10–400 for $\mathrm{N_2O}$, and 1×10^4 to 2×10^4 for $\mathrm{SF_6}$. The value of the metrics is strongly influenced by the horizon, and in many cases, the variation with time horizon is more important than model

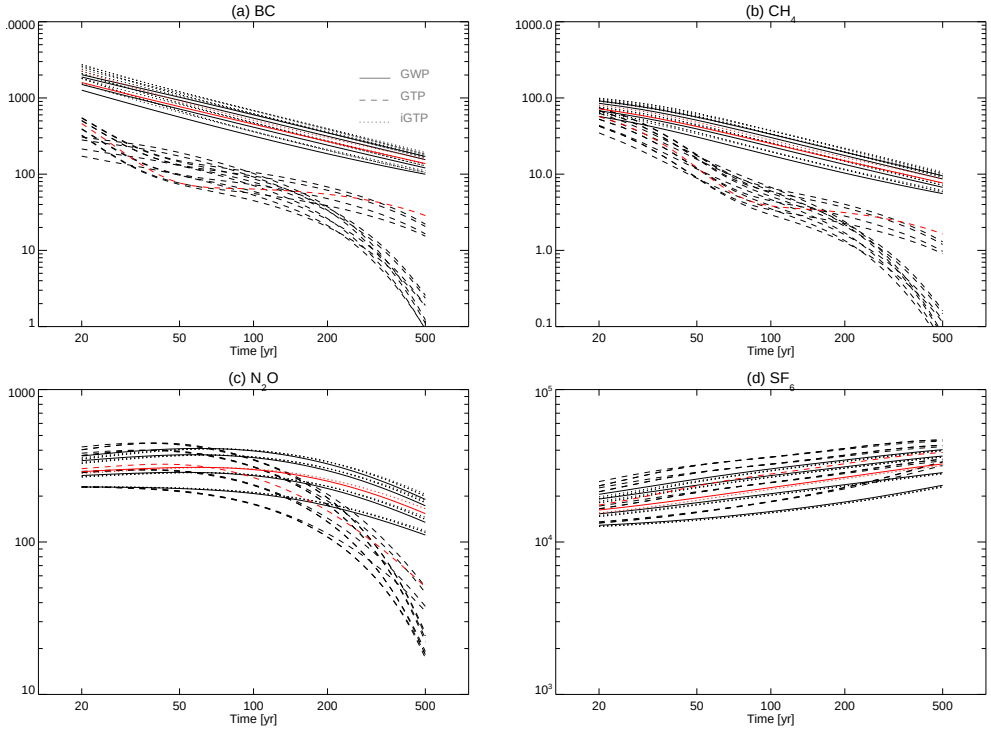

Fig. 3. Evolution of GWP (full line), GTP (dashed line), and iGTP (dotted line) as a function of the time horizon for **(a)** BC, **(b)** CH_4, **(c)** N_2O, and **(d)** SF_6, using different combinations of IRF_{CO_2} and IRF_T. The black curves correspond with all combinations of IRF_{CO_2} distributions (C^4MIP(u), C^4MIP(c), LTMIP, and J13) and IRF_T distributions (CMIP3, CMIP3*, and CMIP5) – the lines shown are the median values of the obtained metric distributions. The red lines are the result of the combination of the reference IRF_{CO_2} J07 and IRF_T BR08. The vertical axis is dimensionless.

variation. For BC and CH_4 the metric values decay strongly as a function of the time horizon, for N_2O they have the tendency to decay slightly as a function of the time horizon, and for SF_6 metric values increase as a function of the time horizon (Tanaka et al., 2009). The GWP and iGTP metric behave in general very similar, but the behaviour of GTP can be rather different. For a specific species, metric, and time horizon, the median values differ in general considerably, up to a factor of two, but the GTPs of BC and CH_4 show variation in the median up to a factor of 10 for time horizons of 500 yr or more.

To clarify more the impact of the IRFs on the metrics, we will separately investigate the impact of variation in IRF_{CO_2} and IRF_T on metrics. The impact will be decomposed in a *deviation* (indicating how much the median value of a metric differs from the case where the reference IRF is used) and a *spread* (indicating how much the 5- and 95-percentile metric values differ from the median).

4.2.1 Impact of variation in CO_2 IRF

Figure 4 shows the impact of IRF_{CO_2} on GWP, GTP, and iGTP. We used different IRF_{CO_2} (J07, C^4MIP(u), C^4MIP(c), LTMIP, and J13), but always the BR08 IRF_T to isolate the changes caused by IRF_{CO_2}.

Figure 4a shows the difference between the median metric value obtained using a specific IRF_{CO_2} and the value obtained using the reference J07. As variation in IRF_{CO_2} only affects the denominator in the expression for GWP, GTP, or iGTP, and as this denominator is equal for all species, the impact from variation in IRF_{CO_2} is identical for all the four species we study here. The LTMIP and J13 IRF_{CO_2} lead to lower values than J07 (around $-25\,\%$ for LTMIP and $-5\,\%$ to $-15\,\%$ for J13). These lower values reflect the fact that the LTMIP and J13 IRF_{CO_2} are higher than the J07 IRF_{CO_2} (see Fig. 1a). The median metric values from C^4MIP(u) and C^4MIP(c) are significantly higher than the J07 values (10–40 %). This is caused by the fact that both C^4MIP IRF_{CO_2} are lower than the J07 IRF_{CO_2}.

Figure 4a also shows that the impact of variation in IRF_{CO_2} is similar for the three metrics (GWP, GTP, and iGTP). The closest agreement can be seen between GWP and iGTP (Peters et al., 2011). Also the variation of the metrics as a function of the time horizon or choice of IRF_{CO_2} is very similar for the three metrics, although the maximum deviation is situated at shorter time horizons for GTP than for GWP and iGTP.

The C^4MIP(u) IRF_{CO_2} gives 10 % higher metric values than the C^4MIP(c) IRF_{CO_2}, and this for all metrics. Joos et al.

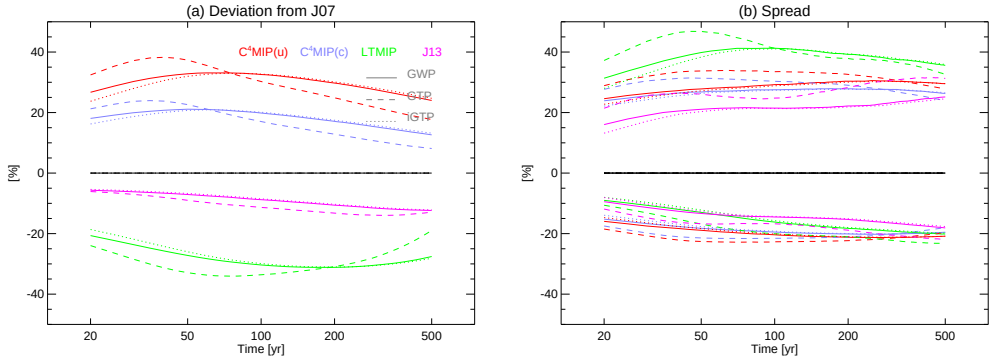

Fig. 4. Impact of variation in IRF_{CO_2} on GWP (full line), GTP (dashed line), and iGTP (dotted line), using the C^4MIP(u) (red), C^4MIP(c) (blue), LTMIP (green), and J13 (purple) IRF_{CO_2}. **(a)** Difference between the median of the obtained metric distribution and the value obtained using the reference J07 IRF_{CO_2}. **(b)** Spread of the obtained metric distribution, indicating the difference between the 5-percentile value and the median value (lower lines), and between the 95-percentile value and median value (upper lines). These impacts are equal for all species (BC, CH_4, N_2O, and SF_6).

(2013, Sect. 4.4.3 and Fig. 7), who investigated the impact of the temperature feedback with one CC-model, found an impact of 13 % on the integrated IRF_{CO_2} at time horizons of 100 and 500 yr for a pulse emission size of 100 Gt[C]. Slightly smaller impacts are found for time horizons shorter than 100 yr or longer than 500 yr.

Figure 4b shows the spread of the metric values, indicating how much the 5- and 95-percentile values differ from the median value. Again, these spreads are identical for all species, and one can see that these spreads do not vary much among the different metrics. The differences fall in the range of -20 to $+40$ %, and are not very sensitive to the value of the time horizon. The LTMIP IRF_{CO_2} induces a slightly more asymmetric spread than the other IRF_{CO_2}, which is most pronounced for short time horizons. This is a consequence of the asymmetric LTMIP IRF_{CO_2}, as can be seen in Fig. 1a.

The variation in the GWP estimates presented here is solely caused by variation in its denominator $AGWP_{CO_2}$, implying that the variation we estimated for GWP, actually also gives the variation in $AGWP_{CO_2}$. Joos et al. (2013, Table 4) indicate spreads for $AGWP_{CO_2}$. Converting their 2σ values for $AGWP_{CO_2}$ into 5- and 95-percentile values gives for $H = 20$, 50, 100, and 500 yr the ranges ± 10, ± 15, ± 18, and ± 21 %, respectively. These values agree well with the impacts we found of -9 to $+16$ %, -13 to $+21$ %, -14 to $+22$ %, and -18 to $+25$ % (see purple full line in Fig. 4b, or later see Fig. 6). Reisinger et al. (2010) have also estimated uncertainties on the $AGWP_{CO_2}$. Their 5–95 % confidence interval values for $AGWP_{CO_2}$ (based on their AOGCM/C^4MIP model evaluation) give -17 to $+19$ %, -23 to $+26$ %, and -25 to $+22$ % for $H = 20$, 100, and 500 yr, respectively. Although they included also the impact of uncertainty in radiative efficiencies, their variations are comparable to our values. In Reisinger et al. (2011) the 5- to 95-percentile range in GWP_{CH_4} and GWP_{N_2O} is estimated to be -15 to $+20$ % for $H = 20$ yr and -20 to $+30$ % for $H = 100$ and 500 yr, which is in fair agreement with our estimates.

4.2.2 Impact of variation in temperature IRF

The GTP and iGTP metric values also depend on IRF_T. We investigate this by using the reference J07 IRF_{CO_2}, but different IRF_T (BR08, CMIP3, CMIP3*, and CMIP5). This variation influences both the numerator and denominator in the expression for GTP and iGTP (see Eqs. 9 to 12). We mainly concentrate on GTP, as iGTP is much less influenced.

Figure 5 shows the impact of variation in IRF_T on GTP. Figure 5a shows the deviation of the median value from the value obtained using the reference IRF_T. In contrast to the impact of IRF_{CO_2}, the impact now differs among species. N_2O and SF_6 show very small variations due to variation in IRF_T, while BC shows a deviation of the median from the reference value in the range of -90 to $+85$ %, and for CH_4 in the range of -90 to $+45$ %. We see, for example, that for BC and CH_4 using the CMIP3, CMIP3*, or CMIP5 IRF_T gives lower metric values with respect to BR08 for the smallest time horizon ($H = 20$ yr), but higher values for $H = 50$ yr, and this is most pronounced for the CMIP5 IRF_T. This behaviour can be explained by noting that GTP_{BC} is the ratio of $AGTP_{BC}$ and $AGTP_{CO_2}$. As BC has a very short lifetime, the time dependence of $AGTP_{BC}$ is very similar to the IRF_T curve in Fig. 2a. On the other hand, because CO_2 has characteristics of a longer lifetime, the time dependence of $AGTP_{CO_2}$ will be more similar to the integrated IRF_T curve in Fig. 2b. For $H = 20$ yr, we see that the CMIP5 IRF_T is much lower than BR08 (determining the numerator), while the integrated CMIP5 IRF_T is similar to BR08 (determining the denominator). This explains why the value for BC at $H = 20$ yr is so low using the CMIP5 IRF_T. The inverse behaviour for $H = 50$ yr is caused by the fact that now the numerator is slightly higher for IRF_T (see Fig. 2a), while the denominator is consistently smaller. The changing relative position of the IRF_T curves is clearly reflected in the GTP metric values. To a lesser extent the same reasoning is true for CH_4, as it still has a relative short lifetime with respect

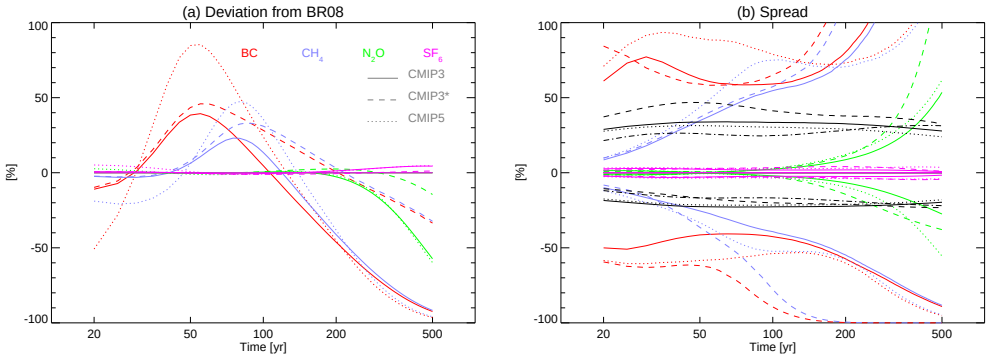

Fig. 5. Impact of variation in IRF_T on GTP for BC (red), CH_4 (blue), N_2O (green), and SF_6 (purple), using the CMIP3 (full line), CMIP3* (dashed line), and CMIP5 (dotted line) IRF_T. **(a)** Difference between the median of the obtained metric distribution and the value obtained using the reference BR08 IRF_T. **(b)** Spread of the obtained metric distribution, indicating the difference between the 5-percentile value and the median value (lower lines), and between the 95-percentile value and median value (upper lines). The black lines show the spread induced by IRF_{CO_2} on GTP from C^4MIP(u) (full line), C^4MIP(c) (dotted line), LTMIP (dashed line), and J13 (dot-dashed line); these lines are identical to the dashed lines in Fig. 4b.

to CO_2. One can note that for time horizons of 200 yr and longer, the curves for BC (red) and CH_4 (blue) have the tendency to coincide. One can also see that for BC and CH_4 and for time horizons between 200 and 500 yr, CMIP3* (dashed line) gives a smaller deviation than CMIP3 or CMIP5.

The generally small deviations for N_2O and SF_6 from BR08 for the time horizons considered are caused by the fact that $AGTP_{N_2O}$ and $AGTP_{SF_6}$, as a function of time, behave similarly to the integrated IRF_T (as long as the horizon is not much longer than the lifetime of the species). CO_2 has a similar dependence on IRF_T (see above). As a consequence, the variations in the numerator and denominator of the GTP expression due to variations in the IRF_T will be similar and largely cancel out in the expression for GTP_{N_2O} and GTP_{SF_6}. As this condition is not fulfilled with N_2O for time horizons longer than 200 yr, GT_{N_2O} starts to deviate from there on.

Figure 5b shows the spread in GTP values due to variation in IRF_T. The amount of spread is strongly dependant on the species and the time horizon. For time horizons up to $H = 100$ yr, BC shows variations in the range of -60 to $+80$ %, and this spread increases drastically for longer time horizons. For CH_4, the spread is smaller than for BC when looking at time horizons of 20 and 50 yr, but rather similar for longer ones. For N_2O, very small ranges are found up to time horizons of 100 yr, but increasing after that. For SF_6 we find small spreads for all time horizons.

For comparing the impact of variation in IRF_{CO_2} and IRF_T, Fig. 5b also shows the impact of IRF_{CO_2} in black (these lines correspond with the dashed lines from Fig. 4b). One can see that the spread in GTP for BC is dominated by IRF_T, and for CH_4 by IRF_{CO_2} at short time horizons ($H = 20$ yr) and by IRF_T at longer time horizons. For N_2O and SF_6 it is dominated by variation in IRF_{CO_2}, except for N_2O at time horizons longer than 200 yr.

Reisinger et al. (2010) present also values for the variation in GTP_{CH_4} for $H = 20$, 100, and 500 yr, i.e. -26 to $+30$ %, -48 to $+77$ %, and -101 to $+172$ %, respectively (we derived the value for $H = 100$ yr from their Table 2). This variation clearly increases as a function of the time horizon, in accordance to our findings.

For iGTP one finds much lower impacts of the variation from IRF_T (not shown), since iGTP is an integrated version of GTP. The deviations are of the order of 5 %, except for BC at $H = 20$ yr using the CMIP5 IRF_T where the deviation reaches -15 %. Spreads are in general smaller than ± 10 %. The much smaller variation in iGTP with respect to GTP, e.g. for BC, can be explained by the fact that the numerator in iGTP is now the integral of the curve shown in Fig. 2a. As the CMIP5 curve up to 20 yr lies partially above and partially below the BR08 curve, the integrals are not that different for $H = 20$ yr. For longer time horizons this difference is even further reduced. Accordingly, also the spread is strongly reduced.

Finally, for two selected IRFs, i.e. the J13 IRF_{CO_2} and the CMIP5 IRF_T, Fig. 6 shows the impact of IRF variation on GWP, GTP, and iGTP for BC, CH_4, N_2O, and SF_6 at specific time horizons of 20, 50, 100, 200, and 500 yr. It shows the impact from variation in IRF_{CO_2}, from variation in IRF_T, and from variation in both IRF_{CO_2} and IRF_T.

4.3 Synthesis of results

The aim of this study was twofold. The first aim was to derive IRF_{CO_2} and IRF_T distributions based on the behaviour of different CC-models and AOGCMs. The second aim was to analyse how variation in these IRFs influences common emission metrics.

The estimate of IRF distributions has been based on simulations from five different model intercomparison exercises, i.e. C^4MIP, LTMIP, and Joos et al. (2013) for estimating

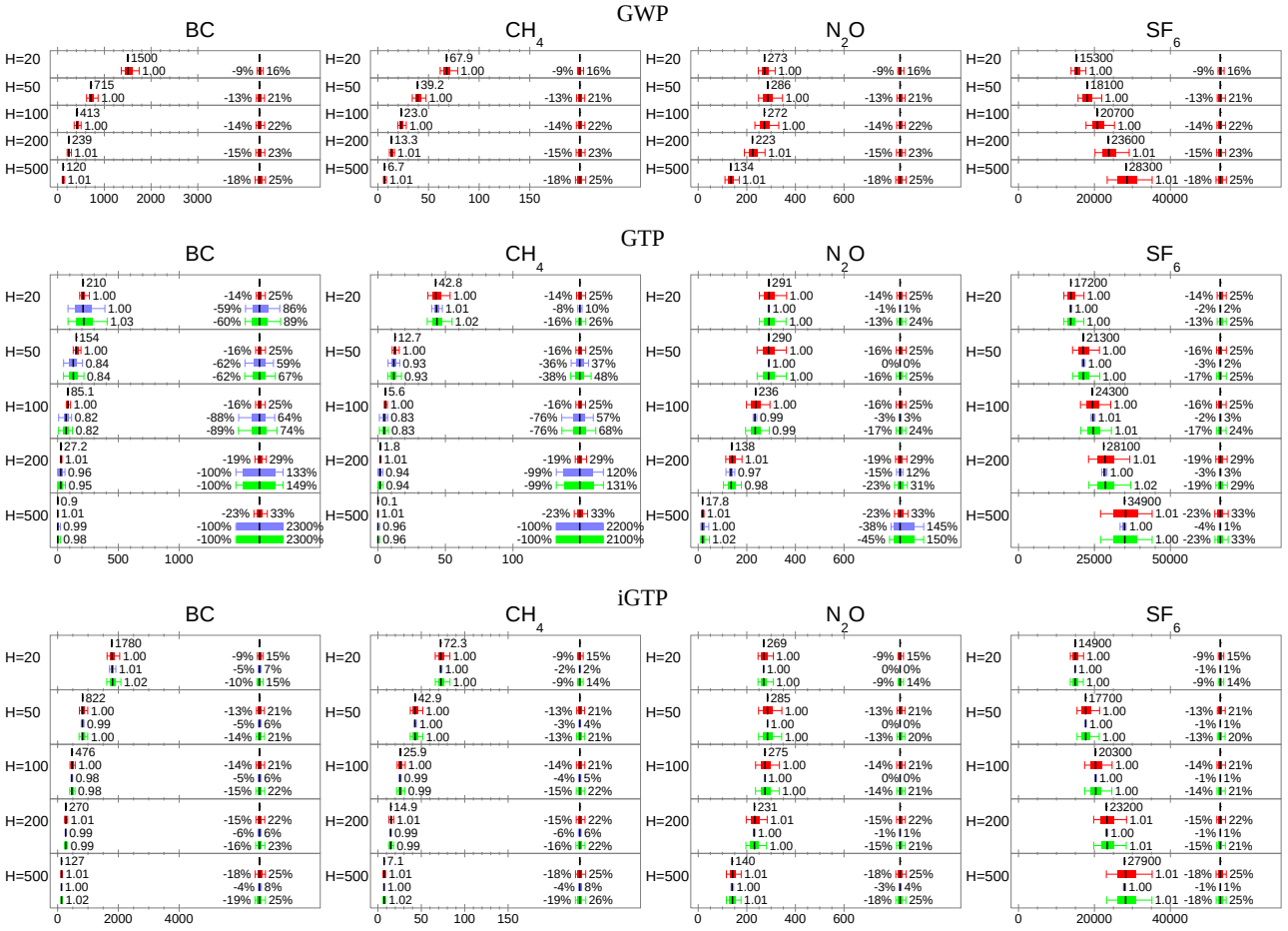

Fig. 6. Impact of variation in J13 IRF_{CO_2} and CMIP5 IRF_T on GWP, GTP, and iGTP values for BC, CH_4, N_2O, and SF_6 for time horizons of 20, 50, 100, 200, and 500 yr. The red bars give the impact of variation in IRF_{CO_2}, the blue bars the impact of variation in IRF_T, and the green bars the impact of variation in both IRF_{CO_2} and IRF_T. For every time horizon, the little black line (top) represents the reference value of the metric using the parameters as given in Tables 3 and 4 in the IRFs – the value itself is indicated to the right of the little line. The left bars give the 5-, 25-, 50-, 75-, and 95-percentile values of the metric (the 50-percentile value is indicated by a black line). The number right of the bar indicates how much the median value deviates from the reference value in relative terms. The right bars indicate the spread with respect to the median value, where again the 5-, 25-, 75-, and 95-percentile values are represented. The numbers (in %) left and right of the bars indicate how much the 5- and 95-percentile values deviate from the median value. The horizontal axis which gives the value of the metric is dimensionless.

IRF_{CO_2} distributions, and CMIP3 and CMIP5 for estimating IRF_T distributions. As reference for comparison we have taken the IRF_{CO_2} from Forster et al. (2007) (in the text noted as J07) and the IRF_T from Boucher and Reddy (2008) (in the text noted as BR08).

The J13 IRF_{CO_2} is similar to the reference J07 IRF_{CO_2}, but the behaviour of the other three derived IRF_{CO_2} is rather different from the reference. The similarity between J07 and J13 reflects similar experimental setups, and differences in experimental setup explain the differences between J07, LTMIP, and C^4MIP. The LTMIP IRF_{CO_2} has a tendency to remain considerably higher than J07, giving similar values to J07 only after 1000 yr. These differences relate to non-linearities caused by the large pulse and different background in LTMIP. The C^4MIP IRF_{CO_2} is considerably lower than the J07 IRF_{CO_2}. The relatively short time series and gradually changing emission scenario in C^4MIP (as opposed to pulse emissions in J07, J13, and LTMIP) lead to a lower confidence in the value of IRF_{CO_2} for short times (below 3–5 yr) and long times (above 500 yr).

Similar spreads in the IRF_{CO_2} are found for J13, C^4MIP(u), and C^4MIP(c). For LTMIP, the width increases slightly stronger as a function of time, and the width of the distribution decreases again for long timescales (100–1000 yr). In general, the order of magnitude of the width of the distributions is similar for all four IRF_{CO_2}.

For IRF_T, the three distributions are generally similar, but also show specific differences. Whereas the CMIP3 results

Table 5. Value of mean vector $\bar{x}$ and covariance matrix $\mathbf{\Sigma}$ in the IRF_{CO_2} distributions (see Eq. 16) derived using C^4MIP, LTMIP, and J13 data. The distribution is for the logarithm of the parameters in IRF_{CO_2}.

	$\log\tau_1$	$\log\tau_2$	$\log\tau_3$	$\log b_1$	$\log b_2$	$\log b_3$
C^4MIP(u)						
$\bar{x}$	5.179	2.480	0.096	−0.172	0.610	0.395
$\mathbf{\Sigma}$						
$\log\tau_1$	0.027	−0.010	−0.005	−0.000	−0.040	0.003
$\log\tau_2$	−0.010	0.033	0.006	0.026	0.002	−0.041
$\log\tau_3$	−0.005	0.006	0.003	0.004	0.010	−0.011
$\log b_1$	−0.000	0.026	0.004	0.026	−0.016	−0.036
$\log b_2$	−0.040	0.002	0.010	−0.016	0.092	−0.002
$\log b_3$	0.003	−0.041	−0.011	−0.036	−0.002	0.070
C^4MIP(c)						
	$\log\tau_1$	$\log\tau_2$	$\log\tau_3$	$\log b_1$	$\log b_2$	$\log b_3$
$\bar{x}$	5.230	2.575	0.100	−0.089	0.493	0.242
$\mathbf{\Sigma}$						
$\log\tau_1$	0.026	−0.009	−0.005	0.002	−0.036	−0.000
$\log\tau_2$	−0.009	0.036	0.008	0.031	0.000	−0.042
$\log\tau_3$	−0.005	0.008	0.004	0.006	0.010	−0.013
$\log b_1$	0.002	0.031	0.006	0.032	−0.016	−0.040
$\log b_2$	−0.036	0.000	0.010	−0.016	0.074	−0.001
$\log b_3$	−0.000	−0.042	−0.013	−0.040	−0.001	0.071
LTMIP						
	$\log\tau_1$	$\log\tau_2$	$\log\tau_3$	$\log b_1$	$\log b_2$	$\log b_3$
$\bar{x}$	5.601	3.517	0.501	0.933	0.139	−0.959
$\mathbf{\Sigma}$						
$\log\tau_1$	0.065	0.030	−0.019	−0.006	−0.014	−0.011
$\log\tau_2$	0.030	0.342	0.054	0.094	−0.106	−0.389
$\log\tau_3$	−0.019	0.054	0.060	0.043	−0.022	−0.102
$\log b_1$	−0.006	0.094	0.043	0.064	−0.038	−0.131
$\log b_2$	−0.014	−0.106	−0.022	−0.038	0.039	0.127
$\log b_3$	−0.011	−0.389	−0.102	−0.131	0.127	0.481
J13						
	$\log\tau_1$	$\log\tau_2$	$\log\tau_3$	$\log b_1$	$\log b_2$	$\log b_3$
$\bar{x}$	5.479	2.913	0.496	0.181	0.401	−0.472
$\mathbf{\Sigma}$						
$\log\tau_1$	0.129	−0.058	0.017	−0.042	−0.004	−0.009
$\log\tau_2$	−0.058	0.167	−0.109	0.072	−0.015	0.003
$\log\tau_3$	0.017	−0.109	0.148	−0.043	0.013	−0.013
$\log b_1$	−0.042	0.072	−0.043	0.090	0.009	0.006
$\log b_2$	−0.004	−0.015	0.013	0.009	0.082	0.013
$\log b_3$	−0.009	0.003	−0.013	0.006	0.013	0.046

Table 6. Value of mean vector $\bar{x}$ and covariance matrix $\mathbf{\Sigma}$ in the IRF_T distributions (see Eq. 16) derived using CMIP3, CMIP3*, and CMIP5 data. The distribution is for the logarithm of the parameters in IRF_T.

	$\log\tau_1$	$\log\tau_2$	$\log f_1$	$\log f_2$
CMIP3				
$\bar{x}$	1.967	4.659	−0.739	−1.612
$\mathbf{\Sigma}$				
$\log\tau_1$	0.056	−0.033	0.012	0.012
$\log\tau_2$	−0.033	0.064	−0.005	0.028
$\log f_1$	0.012	−0.005	0.042	−0.000
$\log f_2$	0.012	0.028	−0.000	0.110
CMIP3*				
	$\log\tau_1$	$\log\tau_2$	$\log f_1$	$\log f_2$
$\bar{x}$	1.980	5.499	−0.714	−1.031
$\mathbf{\Sigma}$				
$\log\tau_1$	0.080	−0.100	0.011	−0.066
$\log\tau_2$	−0.100	0.423	−0.005	0.102
$\log f_1$	0.011	−0.005	0.031	0.011
$\log f_2$	−0.066	0.102	0.011	0.259
CMIP5				
	$\log\tau_1$	$\log\tau_2$	$\log f_1$	$\log f_2$
$\bar{x}$	0.945	4.410	−0.842	−1.154
$\mathbf{\Sigma}$				
$\log\tau_1$	0.089	0.147	0.038	0.034
$\log\tau_2$	0.147	0.701	0.019	0.001
$\log f_1$	0.038	0.019	0.040	0.024
$\log f_2$	0.034	0.001	0.024	0.133

coincide with BR08 for the first 10 yr and CMIP5 is considerably higher than BR08 for the same period, all three derived distributions are very similar in the period 20–100 yr, but below the BR08 value. For long timescales, they all give considerably lower values than BR08. The width of all IRF_T distributions is in general rather similar, becoming larger for longer timescales. The IRF_T have a similar spread in climate sensitivity, i.e. 0.4 K for CMIP3, 0.6 K for CMIP5 and 0.7 K for CMIP3* (5–95 % spread). Although for long timescales the BR08 IRF_T is considerably higher than the new IRF_T, BR08 falls still within the high end of the CMIP3* distribution.

The spread in IRFs has a considerable impact on the values of the GWP, GTP, and iGTP metrics. The impact of the spread in IRF_{CO_2} is very similar for the three emission metrics, and these variations are equal for all studied species (BC, CH_4, N_2O, and SF_6). The main characteristics of the IRF_{CO_2} have a straightforward impact on the emission metrics: the higher LTMIP IRF_{CO_2} gives lower metric values, whereas the lower C^4MIP IRF_{CO_2} give higher metric values. The spread within all the IRF_{CO_2} distributions creates very similar spreads, varying between −20 and +40 % for all metrics.

The GTP and iGTP metrics are also influenced by the spread in the IRF_T. For GTP, the IRF_T-induced spread is

significantly larger than the IRF_{CO_2}-induced spread for short-lived species such as BC for all studied time horizons, and for CH_4 for the longer time horizons. Using the CMIP3* IRF_T for long time horizons, spreads are considerably larger than using the CMIP3 or CMIP5 ones. There are very small differences in the GTP values for N_2O (for time horizons smaller than 200 yr) and SF_6, although IRF_T differs considerably. This is since the IRF_T appears in both the numerator and denominator of the GTP expressions, and the relative long lifetimes of CO_2, N_2O, and SF_6. Due to the integrative character of iGTP, the IRF_T-induced spread is much smaller than for GTP. The IRF_T-induced spread is even smaller than the IRF_{CO_2}-induced spread.

5 Conclusions

We have analysed variations in IRFs for CO_2 (IRF_{CO_2}) and temperature (IRF_T), and quantified the impacts of these variations on common metric values. We found that the variations were important and had a significant effect on metric values. Since we used model intercomparisons for our assessment, the results do not span the full range of uncertainties. Additionally, since only one model intercomparison was designed for metric applications, the variations may be somewhat affected by the specific experimental designs. Our results need to be interpreted in the context of these issues.

Part of the differences between the derived IRFs can be attributed to the type of experiment performed with the CC-models and AOGCMs. Pulse-type experiments as in LTMIP and J13 are very useful to quantify IRF_{CO_2}, but the LTMIP IRF_{CO_2} is biased upwards due to the experimental design and focus on long-term carbon cycle dynamics. This makes the LTMIP distribution less useful for metric applications. The gradual evolution and short length of the CO_2 emission scenario in C^4MIP makes it difficult to uniquely determine the IRF_{CO_2}. Thus, most significance should be placed on the J13 results. The CMIP5 experiment with its abrupt forcing change is in principal very useful to derive IRF_T. However, these experiments also show in general a lower value for the large timescale due to the short length of the simulation. Extending these scenario up to $\sim$ 500 yr would allow us to better constrain the parameters in IRF_T, and especially allow us to use IRF_T for longer times.

Based on this assessment, we would suggest that specific experiments should be used for IRFs with clearly defined experimental setups (as in Joos et al., 2013). It is also possible to estimate the AGTP directly from a pulse emission (as in Joos et al., 2013), and this ensures model consistency. In the case of IRF_T, it is clear that longer experiments are needed to better constrain the long timescales and hence the climate sensitivity. Irrespective of the experimental setups used, our analysis clearly demonstrates that a single model should not be used as the basis of an emission metric. The model mean arguably gives a more reliable estimate than any particular model (chosen at random), and a model intercomparison adds value by providing the model spread. Nevertheless, the use of the presented metric distributions should be taken with care. They represent only estimates of the spreads related to the behaviour of the underlying CC-model or AOGCM, and the model spread may not be indicative of the true uncertainties. The estimates do not take into account other reasons for spread that might impact metric values, such as uncertainties on the lifetime of BC, CH_4, N_2O, or SF_6. One should also be aware that the analysis presented here provides uncertainties when comparing arbitrary species with CO_2, but does not provide uncertainties for the comparison of two non-CO_2 species nor absolute metric values for single species. This has not been discussed, but such an analysis can be performed based on the IRF distributions presented in this work.

Appendix A

Sensitivity tests with a simple CC-model

We performed sensitivity tests to clarify how the IRF_{CO_2} derived from C^4MIP data are influenced by the high CO_2 concentrations in the 21st century (the non-linear regime), and by the almost exponential increase in emissions. For the C^4MIP CC-models, the IRF_{CO_2} that would have been obtained when imposing a small CO_2 emission pulse (and which we will call the *proper* IRF_{CO_2}) is unknown, and this makes it hard to judge whether the derived IRF_{CO_2} agrees well with it. To investigate this, we use a simple CC-model described in Joos et al. (1996), for which we know the proper IRF_{CO_2}.

A1 Impact of non-linearities on IRF_{CO_2}

The CC-model of Joos et al. (1996) contains two non-linearities: one in the expression of the partitioning between CO_2 and total carbon in the mixed layer of the ocean, and one in the expression of the net primary production. We will use the standard version of the CC-model, but also a linearized version of it. The IRF_{CO_2} can be directly derived by imposing a pulse emission in the CC-model. It shows that for small emission pulses, the IRF_{CO_2} found is equal for the standard and linearized versions of the CC-model. For an emission pulse of 100–200 Pg[C], the derived IRF_{CO_2} starts to deviate (see also Joos et al., 2013).

Both with the standard and linearized CC-model, we have generated concentration evolutions using the C^4MIP emission scenario (as we assumed a constant temperature in the CC-model, the experiment is most like C^4MIP(u)). Then we applied the method described in Section 3.2.1 to extract the IRF_{CO_2}, and investigate whether limiting the data period used for the derivation of IRF_{CO_2} up to year 2000, 2025, 2050, or 2100 allows us to retrieve the proper IRF_{CO_2}. Figure A1a shows that for data from the linearized CC-model,

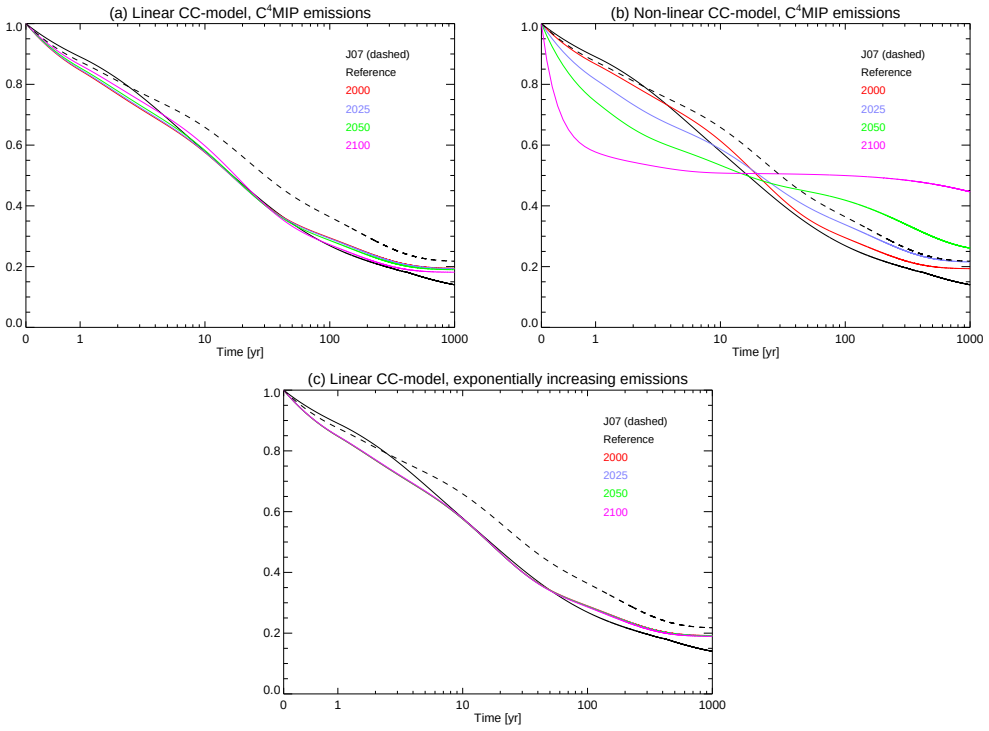

Fig. A1. IRF_{CO_2} derived for the CC-model of Joos et al. (1996), when using data up to year 2000 (red), 2025 (blue), 2050 (green), and 2100 (purple). The solid black line indicates the proper IRF_{CO_2} from this CC-model, and the dashed black line shows the J07 IRF_{CO_2}. **(a)** IRF_{CO_2} derived from data generated with the linearized version of the CC-model forced by C^{4}MIP emissions. **(b)** IRF_{CO_2} derived from data generated with the non-linear CC-model forced by C^{4}MIP emissions. **(c)** IRF_{CO_2} derived from data generated with the linearized version of the CC-model forced by exact exponentially increasing emissions.

the derived IRF_{CO_2} is close to the proper IRF_{CO_2}. The correspondence is better when using more data; however, already when using data up to year 2000, the derived IRF_{CO_2} behaves rather well. For all cases, we see larger deviations for short times (less than 3–5 yr) and long times (more than 500 yr). Figure A1b shows that when the data is generated by the standard non-linear version of the CC-model, one still derives the real IRF_{CO_2} when only data is used up to year 2000, while clear deviations start to be visible when data is used up to year 2025 or later.

A2 Impact of exponentially increasing emissions on IRF_{CO_2}

In a linear system with an exponential forcing, one finds that responses are also exponential (Raupach, 2013). In Appendix B we show theoretically that different IRF_{CO_2} can lead to the same concentration evolution when emissions are exponential. In the C^{4}MIP experiments, the CO_2 emissions increase *almost* exponentially. Here we want to investigate whether this possible ambiguity favours a flat IRF_{CO_2} in our estimation method, similar to the curves shown in Fig. A1b when data up to year 2025 or later is used. To test the impact of such an emission scenario, we have used *exact* exponentially increasing emissions over the period 1750–2100, with a timescale of 60 yr, i.e.

$$E(t) = E_0 \exp \frac{t - 2000\,\mathrm{yr}}{60\,\mathrm{yr}}, \qquad \text{(A1)}$$

where E_0 is the annual emission size in year 2000, for which we have taken a value of 7 Tg[C] yr^{-1} (this emission evolution is in general quite close to the C^{4}MIP emission evolution). The linearized version of the CC-model is then used to calculate the concentration evolution. Figure A1c shows the IRF_{CO_2} derived when using data up to year 2000, 2025, 2050, and 2100. It indicates that the use of exact exponentially increasing emissions does not force the IRF_{CO_2} into a very flat curve.

Appendix B

IRF_{CO_2} and exponentially increasing emissions – a theoretical analysis

B1 Atmospheric CO_2 burden

Imagine CO_2 emissions which increase exponentially with a timescale τ_e, i.e.

$$E_{CO_2}(t) = E_0 \exp \frac{t}{\tau_e}. \tag{B1}$$

The atmospheric burden $B_{CO_2}(t)$ can be written as (see Eq. 3)

$$B_{CO_2}(t) = \int_{-\infty}^{t} \mathrm{IRF}_{CO_2}(t-t')\, E_{CO_2}(t')\, \mathrm{d}t'. \tag{B2}$$

For general functions f and g, one has the equality

$$\int_{-\infty}^{t} f(t-t')\, g(t')\, \mathrm{d}t' = \int_{0}^{\infty} f(t')\, g(t-t')\, \mathrm{d}t'. \tag{B3}$$

Applying this to Eq. (B2), one can show that the atmospheric burden will always be proportional to the exponential emissions, whatever the IRF_{CO_2} is, as

$$\begin{aligned} B_{CO_2}(t) &= \int_{-\infty}^{t} \mathrm{IRF}_{CO_2}(t-t')\, E_0 \exp \frac{t'}{\tau_e}\ \mathrm{d}t' \\ &= \int_{0}^{\infty} \mathrm{IRF}_{CO_2}(t')\, E_0 \exp \frac{t-t'}{\tau_e}\ \mathrm{d}t' \\ &= E_0 \int_{0}^{\infty} \mathrm{IRF}_{CO_2}(t') \exp \frac{t}{\tau_e} \exp \frac{-t'}{\tau_e}\ \mathrm{d}t' \\ &= E_0 \exp \frac{t}{\tau_e} \int_{0}^{\infty} \mathrm{IRF}_{CO_2}(t') \exp \frac{-t'}{\tau_e}\ \mathrm{d}t'. \end{aligned} \tag{B4}$$

If we define Q as

$$Q = \int_{0}^{\infty} \mathrm{IRF}_{CO_2}(t) \exp \frac{-t}{\tau_e}\, \mathrm{d}t, \tag{B5}$$

one can write

$$B_{CO_2}(t) = E_0\, Q \exp \frac{t}{\tau_e}. \tag{B6}$$

This implies that any other IRF_{CO_2} which gives the same value of Q (see Eq. B5) will lead to an identical time evolution of the atmospheric burden. Below we investigate some different functional forms for IRF_{CO_2}, leading all to the same value of Q.

B2 Exponentially decaying IRF_{CO_2}

Imagine an exponentially decaying IRF_{CO_2}, i.e.

$$\mathrm{IRF}_{CO_2}(t) = a_1 \exp \frac{-t}{\tau_1} \quad \text{for} \quad t \geq 0, \tag{B7}$$

and 0 for $t < 0$. Calculating the integral in Eq. (B5), one finds

$$Q = \frac{a_1}{\frac{1}{\tau_1} + \frac{1}{\tau_e}}. \tag{B8}$$

This means that we have one condition for two unknowns (a_1 and τ_1). Often one takes $a_1 = 1$ and then also τ_1 can be deduced. Another option would be to take the limit $\tau_1 \to \infty$, which leads to $a_1 = \frac{Q}{\tau_e}$.

For an IRF_{CO_2} with two exponential modes, i.e.

$$\mathrm{IRF}_{CO_2}(t) = a_1 \exp \frac{-t}{\tau_1} + a_2 \exp \frac{-t}{\tau_2} \quad \text{for} \quad t \geq 0, \tag{B9}$$

and 0 for $t < 0$, one finds

$$Q = \frac{a_1}{\frac{1}{\tau_1} + \frac{1}{\tau_e}} + \frac{a_2}{\frac{1}{\tau_2} + \frac{1}{\tau_e}}. \tag{B10}$$

This gives one condition for the four variables a_1, τ_1, a_2, and τ_2. Imposing the natural condition that $a_1 + a_2 = 1$ still allows for a large degree of freedom in the choice of the parameter values.

B3 Piecewise linear IRF_{CO_2}

For an IRF_{CO_2} of the form

$$\mathrm{IRF}_{CO_2}(t) = a_1 \left(1 - \frac{t}{\tau_1}\right) \quad \text{for} \quad 0 \leq t \leq \tau_1,$$

and 0 elsewhere, one finds

$$Q = a_1 \left(\tau_e + \frac{\tau_e^2}{\tau_1}\left(\exp \frac{-\tau_1}{\tau_e} - 1\right)\right). \tag{B11}$$

This is one condition for two variables (a_1 and τ_1). One can choose $a_1 = 1$, which then allows one to determine τ_1. At the limit $\tau_1 \to \infty$, the solution approaches a constant function with $a_1 = \frac{Q}{\tau_e}$. This is the same limit as one would find in the exponential case.

Acknowledgements. We thank the different modelling groups participating in the CMIP3, C^{4}MIP, LTMIP, CMIP5, and Joos et al. (2013) model intercomparison projects for producing and making available their model output. We thank M. Eby and D. Archer for providing the LTMIP data, P. Friedlingstein for providing the C^{4}MIP data, and F. Joos and R. Roth for providing the Joos et al. (2013) data. We acknowledge the World Climate Research Programme's Working Group on Coupled Modelling, which is responsible for CMIP. For CMIP the US Department of Energy's Program for Climate Model Diagnosis and Intercomparison provides coordinating support and led development of software

infrastructure in partnership with the Global Organization for Earth System Science Portals. This work was partially funded by the US Federal Aviation Administration project Aviation Climate Change Research Initiative (ACCRI). The research leading to these results has received funding from the European Union Seventh Framework Programme (FP7/2007-2013) under grant agreement no. 282688 – ECLIPSE. The authors also wish to acknowledge funding from the Norwegian Research Council.

Edited by: H. Held

References

Aamaas, B., Peters, G. P., and Fuglestvedt, J. S.: Simple emission metrics for climate impacts, Earth Syst. Dynam., 4, 145–170, doi:10.5194/esd-4-145-2013, 2013.

Archer, D., Kheshgi, H., and Maier-Reimer, E.: Multiple timescales for neutralization of fossil fuel CO_2, Geophys. Res. Lett., 24, 405–408, doi:10.1029/97GL00168, 1997.

Archer, D., Eby, M., Brovkin, V., Ridgwell, A., Cao, L., Mikolajewicz, U., Caldeira, K., Matsumoto, K., Munhoven, G., Montenegro, A., and Tokos, K.: Atmospheric lifetime of fossil fuel carbon dioxide, Annu. Rev. Earth Planet. Sci., 37, 117–134, doi:10.1146/annurev.earth.031208.100206, 2009.

Azar, C. and Johansson, D. J. A.: On the relationship between metrics to compare greenhouse gases – the case of IGTP, GWP and SGTP, Earth Syst. Dynam., 3, 139–147, doi:10.5194/esd-3-139-2012, 2012.

Boucher, O. and Reddy, M. S.: Climate trade-off between black carbon and carbon dioxide emissions, Energy Policy, 36, 193–200, doi:10.1016/j.enpol.2007.08.039, 2008.

Boucher, O., Friedlingstein, P., Collins, B., and Shine, K. P.: The indirect global warming potential and global temperature change potential due to methane oxidation, Environ. Res. Lett., 4, 044007, doi:10.1088/1748-9326/4/4/044007, 2009.

Caldeira, K. and Kasting, J. F.: Insensitivity of global warming potentials to carbon dioxide emission scenarios, Nature, 366, 251–253, 1993.

Cao, L., Eby, M., Ridgwell, A., Caldeira, K., Archer, D., Ishida, A., Joos, F., Matsumoto, K., Mikolajewicz, U., Mouchet, A., Orr, J. C., Plattner, G.-K., Schlitzer, R., Tokos, K., Totterdell, I., Tschumi, T., Yamanaka, Y., and Yool, A.: The role of ocean transport in the uptake of anthropogenic CO_2, Biogeosciences, 6, 375–390, doi:10.5194/bg-6-375-2009, 2009.

Eby, M., Zickfeld, K., Montenegro, A., Archer, D., Meissner, K. J., and Weaver, A. J.: Lifetime of anthropogenic climate change: millennial time scales of potential CO_2 and surface temperature perturbations, J. Climate, 22, 2501–2511, doi:10.1175/2008JCLI2554.1, 2009.

Forster, P., Ramaswamy, V., Artaxo, P., Berntsen, T., Betts, R., Fahey, D. W., Haywood, J., Lean, J., Lowe, D. C., Myhre, G., Nganga, J., Prinn, R., Raga, G., Schulz, M., and Dorland, R. V.: Changes in atmospheric constituents and in radiative forcing, in: Climate change 2007: the physical science basis. Contribution of working group I to the fourth assessment report of the intergovernmental panel on climate change, edited by: Solomon, S., Qin, D., Manning, M., Chen, Z., Marquis, M., Averyt, K., Tignor, M. M. B., and Miller, H. L., Chap. 2, 129–234, Cambridge University Press, Cambridge, UK and New York, NY, USA, 2007.

Friedlingstein, P., Cox, P., Betts, R., Bopp, L., von Bloh, W., Brovkin, V., Cadule, P., Doney, S., Eby, M., Fung, I., Bala, G., John, J., Jones, C., Joos, F., Kato, T., Kawamiya, M., Knorr, W., Lindsay, K., Matthews, H. D., Raddatz, T., Rayner, P., Reick, C., Roeckner, E., Schnitzler, K.-G., Schnur, R., Strassmann, K., Weaver, A. J., Yoshikawa, C., and Zeng, N.: Climate-carbon cycle feedback analysis: results from the C^4MIP model intercomparison, J. Climate, 19, 3337–3353, 2006.

Fuglestvedt, J. S., Berntsen, T. K., Godal, O., Sausen, R., Shine, K. P., and Skodvin, T.: Metrics of climate change: Assessing radiative forcing and emission indices, Clim. Change, 58, 267–331, doi:10.1023/A:1023905326842, 2003.

Fuglestvedt, J. S., Shine, K. P., Berntsen, T., Cook, J., Lee, D. S., Stenke, A., Skeie, R. B., Velders, G. J. M., and Waitz, I. A.: Transport impacts on atmosphere and climate: Metrics, Atmos. Environ., 44, 4648–4677, doi:10.1016/j.atmosenv.2009.04.044, 2010.

Gillett, N. P. and Matthews, H. D.: Accounting for carbon cycle feedbacks in a comparison of the global warming effects of greenhouse gases, Environ. Res. Lett., 5, 034011, doi:10.1088/1748-9326/5/3/034011, 2010.

Gloor, M., Sarmiento, J. L., and Gruber, N.: What can be learned about carbon cycle climate feedbacks from the CO_2 airborne fraction?, Atmos. Chem. Phys., 10, 7739–7751, doi:10.5194/acp-10-7739-2010, 2010.

Hansen, J. E. and Sato, M.: Paleoclimate implications for human-made climate change, in: Climate change: inferences from Paleoclimate and regional aspects, edited by: Berger, A., Mesinger, F., and Šijački, D., Chap. 2, 21–47, Springer, doi:10.1007/978-3-7091-0973-1_2, 2012.

Hansen, J., Sato, M., Ruedy, R., Nazarenko, L., Lacis, A., Schmidt, G., Russell, G., Aleinov, I., Bauer, M., Bauer, S., Bell, N., Cairns, B., Canuto, V., Chandler, M., Cheng, Y., Genio, A. D., Faluvegi, G., Fleming, E., Friend, A., Hall, T., Jackman, C., Kelley, M., Kiang, N., Koch, D., Lean, J., Lerner, J., Lo, K., Menon, S., Miller, R., Minnis, P., Novakov, T., Oinas, V., Perlwitz, J., Perlwitz, J., Rind, D., Romanou, A., Shindell, D., Stone, P., Sun, S., Tausnev, N., Thresher, D., Wielicki, B., Wong, T., Yao, M., and Zhang, S.: Efficacy of climate forcings, J. Geophys. Res., 110, D18104, doi:10.1029/2005JD005776, 2005.

Hasselmann, K., Sausen, R., Maier-Reimer, E., and Voss, R.: On the cold start problem in transient simulations with coupled atmosphere-ocean models, Clim. Dynam., 9, 53–61, 1993.

Hooss, G., Voss, R., Hasselmann, K., Maier-Reimer, E., and Joos, F.: A nonlinear impulse response model of the coupled carbon cycle-climate system (NICCS), Clim. Dynam., 18, 189–202, 2001.

Joos, F., Bruno, M., Fink, R., Siegenthaler, U., Stocker, T. F., Quéré, C. L., and Sarmiento, J.: An efficient and accurate representation of complex oceanic and biospheric models of anthropogenic carbon uptake, Tellus, 48B, 397–417, doi:10.1034/j.1600-0889.1996.t01-2-00006.x, 1996.

Joos, F., Roth, R., Fuglestvedt, J. S., Peters, G. P., Enting, I. G., von Bloh, W., Brovkin, V., Burke, E. J., Eby, M., Edwards, N. R., Friedrich, T., Frölicher, T. L., Halloran, P. R., Holden, P. B., Jones, C., Kleinen, T., Mackenzie, F. T., Matsumoto, K., Meinshausen, M., Plattner, G.-K., Reisinger, A., Segschneider, J., Shaffer, G., Steinacher, M., Strassmann, K., Tanaka, K., Timmermann, A., and Weaver, A. J.: Carbon dioxide and climate im-

pulse response functions for the computation of greenhouse gas metrics: a multi-model analysis, Atmos. Chem. Phys., 13, 2793–2825, doi:10.5194/acp-13-2793-2013, 2013.

Knutti, R.: The end of model democracy?, Climatic Change, 102, 395–404, doi:10.1007/s10584-010-9800-2, 2010.

Li, S. and Jarvis, A.: Long run surface temperature dynamics of an A-OGCM: the HadCM3 4×CO_2 forcing experiment revisited, Clim. Dynam., 33, 817–825, doi:10.1007/s00382-009-0581-0, 2009.

Nakicenovic, N., Alcamo, J., Davis, G., de Vries, B., Fenhann, J., Gaffin, S., Gregory, K., Grübler, A., Jung, T. Y., Kram, T., Rovere, E. L. L., Michaelis, L., Mori, S., Morita, T., Pepper, W., Pitcher, H., Price, L., Riahi, K., Roehrl, A., Rogner, H.-H., Sankovski, A., Schlesinger, M., Shukla, P., Smith, S., Swart, R., van Rooijen, S., Victor, N., and Dadi, Z.: Emissions scenarios, Cambridge University Press, Cambridge, UK and New York, NY, USA, 2000.

Olivié, D. and Stuber, N.: Emulating AOGCM results using simple climate models, Clim Dynam., 35, 1257–1287, doi:10.1007/s00382-009-0725-2, 2010.

Olivié, D. J. L., Peters, G. P., and Sain-Martin, D.: Atmospheric response time scales estimated from AOGCM experiments, J. Climate, 25, 7956–7972, doi:10.1175/JCLI-D-11-00475.1, 2012.

Peters, G. P., Aamaas, B., Berntsen, T., and Fuglestvedt, J. S.: The integrated global temperature change potential (iGTP) and relationships between emission metrics, Environ. Res. Lett., 6, 044021, doi:10.1088/1748-9326/6/4/044021, 2011.

Plattner, G.-K., Knutti, R., Joos, F., Stocker, T. F., von Bloh, W., Brovkin, V., Cameron, D., Driesschaert, E., Dutkiewicz, S., Eby, M., Edwards, N. R., Fichefet, T., Hargreaves, J. C., Jones, C. D., Loutre, M. F., Matthews, H. D., Mouchet, A., Müller, S. A., Nawrath, S., Price, A., Sokolov, A., Strassmann, K. M., and Weaver, A. J.: Long-term climate commitments projected with climate-carbon cycle models, J. Climate, 21, 2721–2751, doi:10.1175/2007JCLI1905.1, 2008.

Prather, M. J.: Lifetimes and time scales in atmospheric chemistry, Phil. Trans. R. Soc. A, 365, 1705–1726, doi:10.1098/rsta.2007.2040, 2007.

Prather, M. J., Holmes, C. D., and Hsu, J.: Reactive greenhouse gas scenarios: Systematic exploration of uncertainties and the role of atmospheric chemistry, Geophys. Res. Lett., 39, L09803, doi:10.1029/2012GL051440, 2012.

Ramaswamy, V., Boucher, O., Haigh, J., Hauglustaine, D., Haywood, J., Myhre, G., Nakajima, T., Shi, G., and Solomon, S.: Radiative forcing of climate change, in: Climate Change 2001: The Scientific Basis. Contribution of Working Group I to the Third Assessment Report of the Intergovernmental Panel on Climate Change, edited by: Houghton, J., Ding, Y., Griggs, D. J., Noguer, M., der Linden, P. J. V., Dai, X., Maskell, K., and Johnson, C. A., Chap. 6, 349–416, Cambridge University Press, 2001.

Randall, D. A., Wood, R. A., Bony, S., Colman, R., Fichefet, T., Fyfe, J., Kattsov, V., Pitman, A., Shukla, J., Srinivasan, J., Stouffer, R. J., Sumi, A., and Taylor, K. E.: Climate models and their evaluation, in: Climate change 2007: the physical science basis. Contribution of working group I to the fourth assessment report of the intergovernmental panel on climate change, edited by: Solomon, S., Qin, D., Manning, M., Chen, Z., Marquis, M., Averyt, K., Tignor, M. M. B., and Miller, H. L., Chap. 8, 589–662, Cambridge University Press, Cambridge, UK and New York, NY, USA, 2007.

Raupach, M. R.: The exponential eigenmodes of the carbon-climate system, and their implications for ratios of responses to forcings, Earth Syst. Dynam., 4, 31–49, doi:10.5194/esd-4-31-2013, 2013.

Reisinger, A., Meinshausen, M., Manning, M., and Bodeker, G.: Uncertainties of global warming metrics: CO_2 and CH_4, Geophys. Res. Lett., 37, L14707, doi:10.1029/2010GL043803, 2010.

Reisinger, A., Meinshausen, M., and Manning, M.: Future changes in global warming potentials under representative concentration pathways, Environ. Res. Lett., 6, 024020, doi:10.1088/1748-9326/6/2/024020, 2011.

Sausen, R. and Schumann, U.: Estimates of the climate response to aircraft CO_2 and NO_x emissions scenarios, Climatic Change, 44, 27–58, 2000.

Seinfeld, J. H. and Pandis, S. N.: Atmospheric chemistry and physics: from air pollution to climate change, Wiley, New York, USA, 2nd Edn., 2006.

Shine, K. P., Derwent, R. G., Wuebbles, D. J., and Morcrette, J.-J.: Radiative forcing of climate, in: Climate change: the IPCC scientific assessment, edited by: Houghton, J. T., Jenkins, G. J., and Ephraums, J. J., Chap. 2, 41–68, Cambridge University Press, 1990.

Shine, K. P., Fuglestvedt, J., Hailemariam, K., and Stuber, N.: Alternatives to the global warming potential for comparing climate impacts of emissions of greenhouse gases, Climatic Change, 68, 281–302, doi:10.1007/s10584-005-1146-9, 2005.

Shine, K. P., Berntsen, T. K., Fuglestvedt, J. S., Skeie, R. B., and Stuber, N.: Comparing the climate effect of emissions of short- and long-lived climate agents, Phil. Trans. R. Soc. A, 365, 1903–1914, doi:10.1098/rsta.2007.2050, 2007.

Solomon, S., Qin, D., Manning, M., Chen, Z., Marquis, M., Averyt, K., Tignor, M. M. B., and Miller, H. L. (Eds.): Climate change 2007: the physical science basis. Contribution of working group I to the fourth assessment report of the intergovernmental panel on climate change, Cambridge University Press, Cambridge, UK and New York, NY, USA, 996 pp., 2007.

Tanaka, K., O'Neill, B. C., Rokityanskiy, D., Obersteiner, M., and Tol, R. S. J.: Evaluating Global Warming Potentials with historical temperature, Climatic Change, 96, 443–466, 2009.

Tanaka, K., Peters, G. P., and Fuglestvedt, J. S.: Policy Update: Multicomponent climate policy: why do emission metrics matter?, Carbon Management, 1, 191–197, 2010.

Tarantola, A.: Inverse problem theory and methods for model parameter estimation, Society for Industrial and Applied Mathematics, Philadelphia, 342 pp., 2005.

Taylor, K. E., Stouffer, R. J., and Meehl, G. A.: An overview of CMIP5 and the experiment design, B. Am. Meteorol. Soc., 93, 485–498, doi:10.1175/BAMS-D-11-00094.1, 2012.

Wigley, T. M. L.: A simple inverse carbon cycle model, Global Biochem. Cy., 5, 373–382, doi:10.1029/91GB02279, 1991.

Wuebbles, D. J., Jain, A. K., Patten, K. O., and Grant, K. E.: Sensitivity of direct global warming potentials to key uncertainties, Climatic Change, 29, 265–297, 1995.